Salt detachment deformation:

The influence of salt thickness and proximity on structural geometry

Thesis submitted in accordance with the requirements of the University of Adelaide for an Honours Degree in Geology

Lewis Maxwell

November 2012

THE UNIVERSITY of ADELAIDE

ABSTRACT

Structural style above detachment zones has been related to thickness and proximity to the basal detachment layer. Fieldwork, structural measurements and seismic interpretation of evaporite horizons in the Amadeus Basin, Central Australia, have given insight into the impact of salt properties on structural geometry of surrounding rocks during compressional deformation. The lower Gillen Member of the Bitter Springs Formation has acted as a detachment horizon since the Late Proterozoic. Paleo-stress orientations, calculated from conjugate fracture sets in outcrop, express the mechanical detachment of younger packages via a 90˚ rotation in maximum horizontal stress. Synformal deflection beneath the Ross River Syncline has evacuated salt to the north, providing a greater amount of compensation for compressive stresses in the detachment horizon. Vertical dip-slip displacement along thrust faults has been sufficient enough to exhume basal sedimentary units where grounding between competent layers has occurred as a result of lateral salt exhaustion. Aspect ratios of folds indicate that a decrease in both amplitude, wavelength and arc length can be attributed to the proximity of the layer to a detachment horizon. Fold geometry consists of small-scale isoclinal and large-scale tight folding, thereby increasing geometrical complexity toward the detachment horizon. Detachment of overriding layers has also appeared to eliminate fold vergence.

KEYWORDS

Salt detachment, structural geometry, evaporite, deformation, Amadeus Basin, Bitter Springs Formation.

TABLE OF CONTENTS

LIST OF FIGURES AND TABLES

INTRODUCTION

Present-day deepwater fold and thrust belts are becoming a popular target for petroleum exploration due to the increasing oil price and advances in drilling technology in deepwater settings (>2000m) (Trudgill *et al.* 1999, Morley *et al.* 2011). For example offshore Borneo - Southeast Asia, Gulf of Mexico, and the Bight Basin, South Australia (Trudgill *et al.* 1999, Li *et al.* 2004, Morley *et al.* 2011). These provinces consist of a series of hanging wall antiforms stacked on top of each other by large fore-thrusts that initiate from a detachment layer during compression (Morley *et al.* 2011). A detachment layer causes a very low cohesive force at the interface between itself and the surrounding layers of rock due to a contrast in competence and thickness (Dahlstrom 1990, Mitra 2003). Generally, a thin, incompetent layer of salt (evaporite) or over-pressured shale is overlain by a thick, competent sandstone or carbonate (Mitra 2003, Rowan *et al.* 2004). When a package of rocks such as this is subject to compressive forces generated by gravitational stresses, far-field stresses, or a combination of both, low cohesion between the layers causes large amounts of slip to occur, as well as folding of competent layers and flow of detachment layers from beneath synforms into the cores of antiforms (Dahlstrom 1990, Mitra 2003). The structures that form as a result are geometrically more complicated than fold styles defined by (Fleuty 1964) (Figure 1).

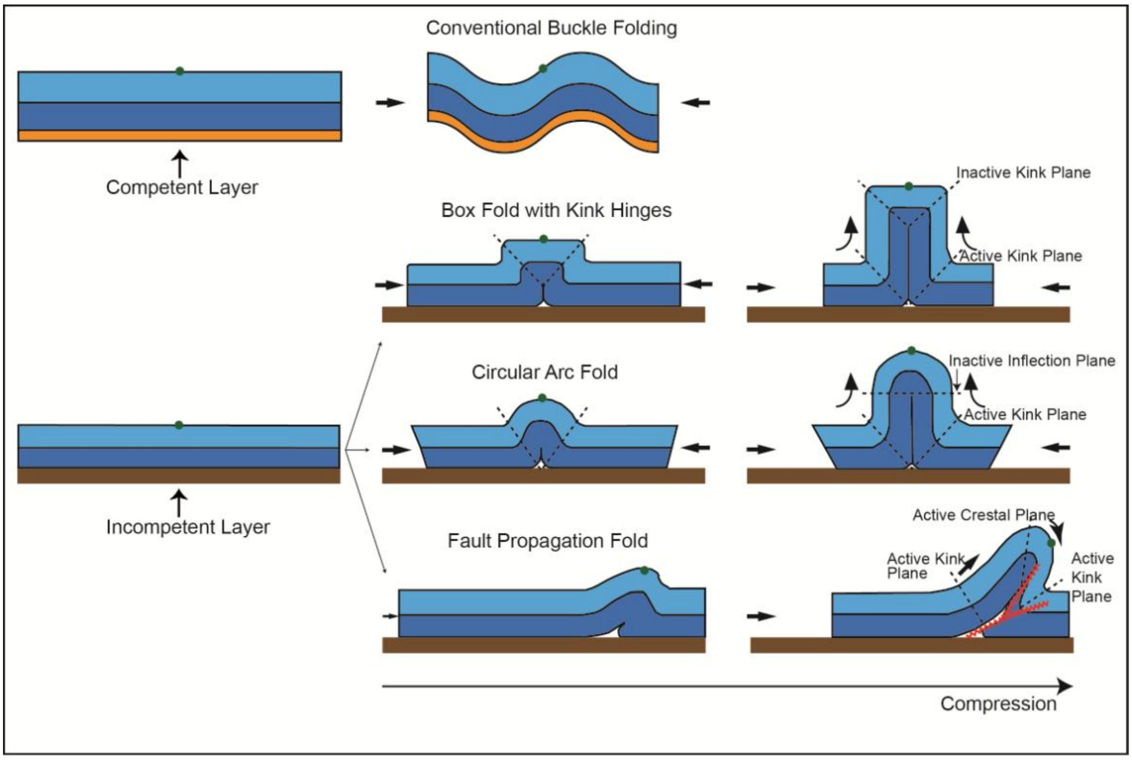

Figure 1. Schematic representation of the comparison between packages of rocks which deform from compressive stresses. If an incompetent basal detachment is present, overlying layers will slip along it producing structures such as box folds, circular arc folds and fault propagation folds. Adapted from Dahlstrom 1990.

Present-day detachment zones can be found in regions that are proximal to deltas, where pro-delta sequences of muds or salts are being covered in outwash river sediments (Trudgill *et al.* 1999, Loncke *et al.* 2006). Areas, such as the Gulf of Mexico and West African margin are referred to as having present-day salt detachment zones, which form a linked system of extension in the delta top and compression in the delta toe, where the formation of deepwater fold and thrust belts occur (King *et al.* 2009) (Figure 2).

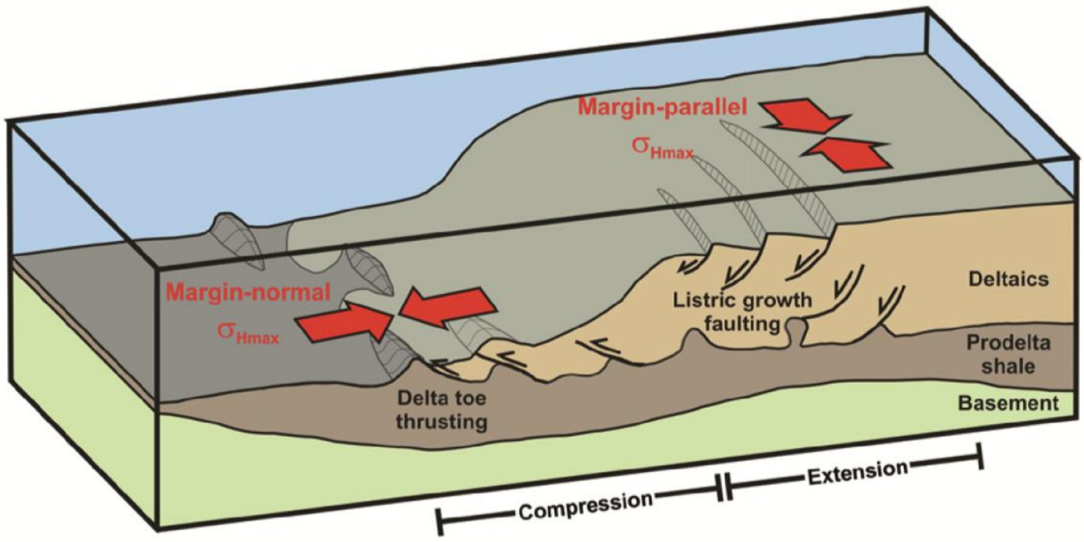

Figure 2. Conventional structure of a current day offshore delta system. Pro-delta muds and shales are overlain by competent layers of rock. Extension in the delta top causes listric normal faults and compression in the delta toe forms a fold and thrust belt. From (King *et al.* 2010).

The Bitter Springs Formation in the Amadeus Basin, Central Australia, contains evaporite horizons within the lower Gillen Member (Figure 3) (Wells *et al.* 1970, Stewart 1979, Shaw & Etheridge 1991) (Figure 3). During compressional deformation, the salt has absorbed compressional stresses through pervasive thrust faulting, as well as flowing from beneath synform hinges into the cores of antiforms.

These evaporite horizons were deposited in the lower Gillen Member of the Bitter Springs Formation following shallowing and isolation of marine shelf deposits during the Neoproterozoic (Lindsay 1999). This caused isolation and a subsequent super-saline environment, thus deposition of evaporites occurred. Following this, tectonic uplift (Korsch & Lindsay 1989, Shaw & Etheridge 1991, Lindsay 1999) or salt diapirism (Kennedy 1993) caused the Areyonga Movement, which produced a wide-spread unconformity between the Bitter Springs Formation and the overlying Areyonga Formation (Figure 3), that contains glacial diamictites equivalent to the Sturtian glacial event (Preiss *et al.* 1978). Deeper water shales of the Aralka Formation were then deposited followed by the Souths Range Movement, which caused uplift and deposition of the Pioneer Sandstone and Olympic Formation (Lindsay 1989). The Olympic Formation is equivalent to the Marinoin glacial event (Preiss *et al.* 1978). Marine transgression followed, resulting in deposition of shale in the Pertatataka Formation, before regression caused shallower sequences of dolomite and sandstone to be deposited as the Julie Formation. A disconformity marks the boundary between the Julie Formation and the Arumbera Sandstone (Walter *et al.* 1995). This boundary marks the Petermann Orogeny ~ 540 – 600 Ma (Wells *et al.* 1970, Shaw & Etheridge 1991, Walter *et al.* 1995). Deposition of remaining overlying formations, such as the Arumbera Sandstone and, Giles Creek Dolomite (Figure 3), were deposited after the Petermann Orogeny until the termination of the most recent tectonic event in the basin - the Alice Springs Orogeny ~ 320 Ma (Ozimic *et al.* 1986, Shaw & Etheridge 1991, Walter *et al.* 1995, Flöttmann & Hand 1999, Marshall & Wiltshire 2007b).

Rheological properties of salt remain constant through time, therefore a salt detachment layer can be active throughout multiple tectonic events (Rowan *et al.* 2004). It is inferred that the Bitter Springs Formation has acted as a detachment throughout its entire tectonic history (Wells *et al.* 1970, Stewart 1979).

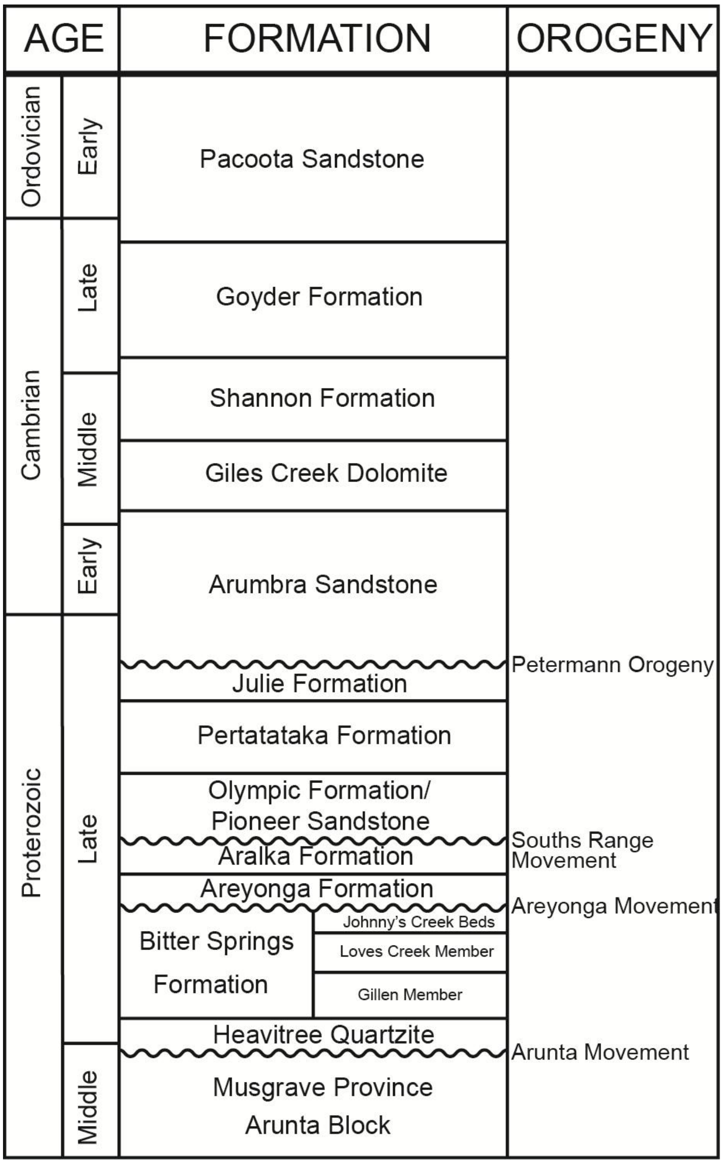

Figure 3. Composite stratigraphic section for the Amadeus Basin, Central Australia (Weste 1990). Adapted from (Skotnicki *et al.* 2008).

In this study, regional seismic data and field data from the Amadeus Basin were studied to identify fold and fault geometries. Seismic images, cross-sections and outcrop were utilised to measure aspect ratios of folds, as well as to calculate shortening amounts. These data have been recorded with respect to thickness of, and distance from, the Gillen Member evaporites in the Bitter Springs Formation. This will gain an overall understanding of the impact of heterogeneities in the detachment layer on structural style which will, in turn, reduce the risk of hydrocarbon exploration in geologically similar settings.

BACKGROUND

An introduction to detachment zones

When a package of rocks is subject to stress, it will undergo deformation that is typical of the orientation of that particular stress (Twiss & Moores 1992). The competency of a layer of rocks will determine how the rocks will deform (Twiss & Moores 1992). A detachment layer is an incompetent sequence of rocks, usually salt (evaporite) or over-pressured shale, that provides a low cohesive force between over and under-lying competent layers of rocks (Dahlstrom 1990, Mitra 2003). Low cohesion between layers causes large amounts of slip, as well as folding during compressional deformation; resulting in unconventional structural styles stratigraphically above the detachment layer (Dahlstrom 1990, Mitra 2003) (Figure 1).

The general structure of a detachment zone consists of a low-cohesive basal layer overlain by thick packages of competent rocks (Rowan *et al.* 2004, Morley *et al.* 2011). These overlying sequences will form fold and thrust belts when subject to compressive forces (Figure 2). Provinces such as this are currently forming offshore in major deltas (e.g. Gulf of Mexico, Northwest Borneo, West Africa and the South Caspian Sea) (Morley *et al.* 2011). Present-day salt detachment locations can be seen on Figure 3.

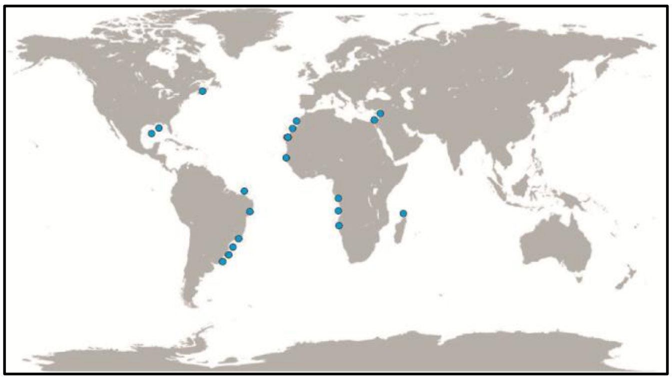

Figure 4. Geographical locations of current day salt detachment zones (blue circle). Adapted from Morley *et al.* 2011.

For the purposes of this study, differentiation between present-day and paleo-detachment zones is outlined, as the Amadeus Basin contains evaporite horizons in the Bitter Springs Formation that have acted as detachment layers throughout the tectonic history of the basin (Wells *et al.* 1970, Stewart 1979) (Figure 3). It has therefore been utilised as an analogue for salt detachment deformation.

Salt Properties

In the sub-surface, sequences of evaporite horizons referred to as salt are not strictly composed completely of the minerals halite, gypsum and anhydrite (Hudec & Jackson 2007). They are often associated with carbonates, chert and some siliciclastic sediments (Hudec & Jackson 2007). Here, we refer to 'salt' as these heterogeneous sequences of halite, gypsum and anhydrite rich sediments.

The rheological properties of salt yield an absence of shear strength. Therefore salt will act like a fluid and flow when it is subject to shear stresses (Rowan *et al.* 2004, Hudec & Jackson 2007). These rheological properties will remain constant through time, and hence, a salt detachment layer will be active throughout multiple tectonic events

(Rowan *et al.* 2004). Shale detachments differ from this, as de-watering processes will eliminate over-pressure in shales and remove its ability to flow (Morley & Guerin 1996).

Salt flow during compressional deformation initiates from accommodation space problems between competent layers of rock. Synchronous sliding and buckling of overlying layers forces the evacuation of salt from beneath synforms into antiform cores, known as synformal deflection, after Mitra 2003 (Figure 5b). This process is indicative of early salt tectonics e.g. Nile delta (Tingay *et al.* 2010).

Another consequence that arises when a layer with no shear stress is present in a system is near-field deformation (Davis & Engelder 1985). A detachment layer will decouple overlying rocks from the regional stress field, thus, the structures that form are not a direct result of tectonic stresses for instance, but instead, the result of local stresses such as gravity sliding (Morley & Guerin 1996).

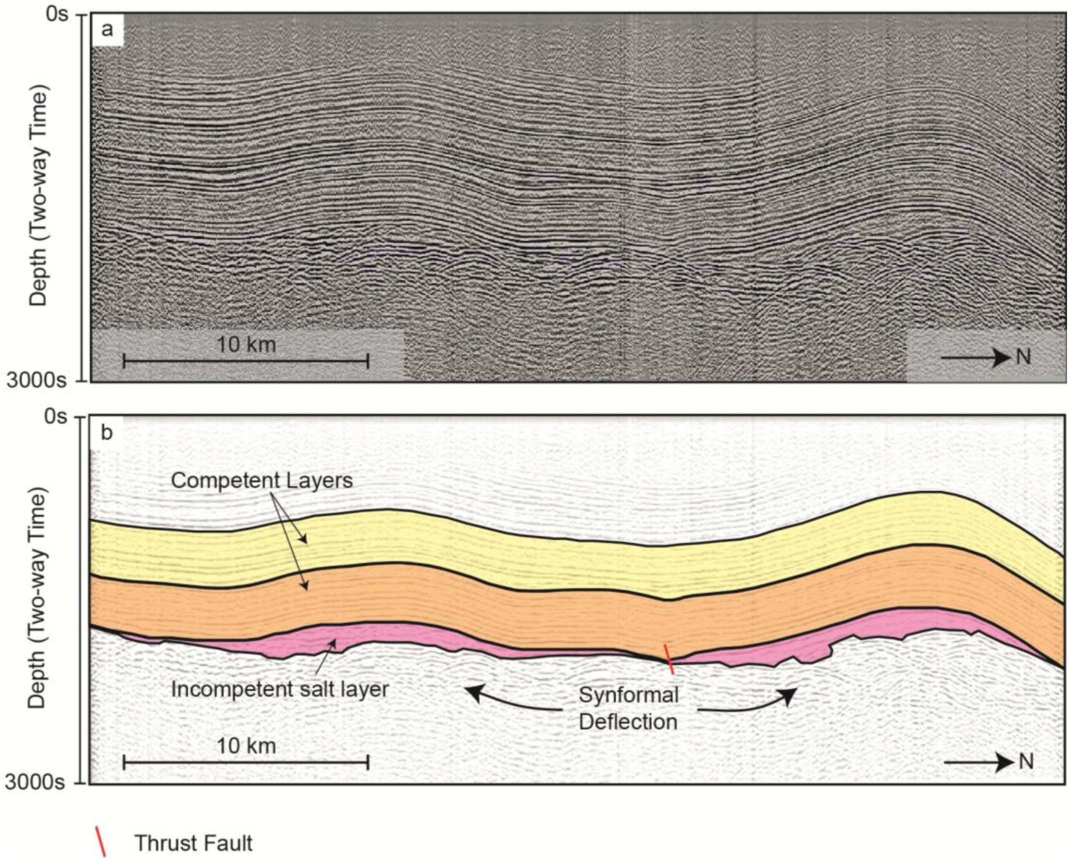

Figure 5. Synformal deflection (Mitra 2003). a) Seismic line P80-11 from the Amadeus Basin (Figure 7a). b) Interpretation showing an example of synformal deflection (Mitra 2003), illustrating the evacuation of the incompetent salt units of the Gillen Member from beneath the synformal structure into the cores of adjacent antiforms.

Not only do structures form in alternate orientations to the stress field, but the overall shortening experienced by the region is greatly compensated for in the basal detachment layer (Morley *et al.* 2011). Salt detachments have been documented to cause shortening amounts of up to 100 km (Morley *et al.* 2011). The mechanism by which it does this is through pervasive folding and faulting compared to the surrounding competent layers.

Detachment-related structures

During compression, a salt detachment will interfere with the development of conventional folds and thrusts. The main mechanism of doing this is through the development of detachment folds (Mitra 2003).

Initial compression above a detachment layer will cause rocks to fold concentrically, resulting in a convergence of the radii of curvature, thus forming a cuspate geometry (Mitra 2003) (Figure 6a). This geometry results in a space problem in the antiform cores. To compensate for this, the detachment layer will buckle, forming disharmonic folds (De Sitter 1964) (Figure 6b).

As the amount of shortening increases, a second common detachment fold forms - lift-off folds (Mitra 2003) . Lift-off folds contain parallel geometries in their outer cores. However, isoclinal folding of the basal detachment occurs in the inner cores. This increases the complexity of fold geometries (Mitra 2003).

Geometrical complexity of folds continues to increase as the amount of shortening increases, leading to detached lift-off folds (Mitra 2003). Detached lift-off folds will cause isoclinal geometries in competent layers within the hinge of folds.

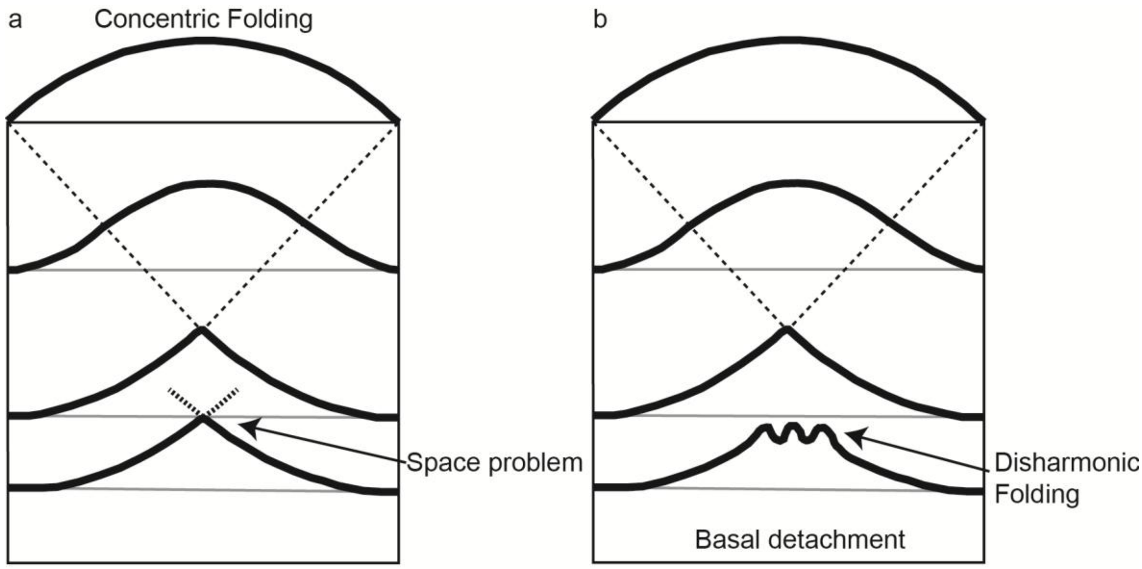

Figure 6. Compressional deformation in detachment zones causes concentric folding of competent layers of rock with parallel geometries in their outer arc. a) A cuspate geometry causes space problems in the cores of concentric antiforms, thus, for competent rocks, this model would be inaccurate. However, b) illustrates a basal detachments' ability to form disharmonic folds to accommodate for this. Adapted from (Mitra 2003).

Heterogeneities in the detachment layer

The aim of this study is to outline how heterogeneities in the basal detachment layer, such as thickness and proximity, have on structural style. To demonstrate this, two case studies on areas that are structurally similar to the Amadeus Basin analogue have been presented.

LOWER CONGO BASIN – ASTRID THRUST BELT

The Astrid Thrust Belt is located in the Lower Congo Basin on the west side of the African continent and was formed in Aptian times in the Early Cretaceous when gentle, west verging antiforms were formed by gravity-driven shortening (Morley & Guerin 1996, Jackson *et al.* 2008). The detachment lithology is salt, and comprises a thin basal layer in the fold and thrust belt, where it is overlain by thick sedimentary sequences of Congo fan deposits (Jackson *et al.* 2008). The tectonic 'trigger' (Morely 2011) which caused near-field deformation in the system was uplift as a consequence of crustal deflection (epirogenic) in the Late Cretaceous (Jackson *et al.* 2008). This uplift caused down dip compression and caused a landward propagating fold and thrust belt (Jackson *et al.* 2008).

In this example, a thin detachment layer was interpreted to mean that pre-existing structures in the area, such as salt walls and diapirs, had a greater affect on the resulting geometry of the Astrid thrust belt (Jackson *et al.* 2008). This resulted in regular spaced thrust faults with similar strikes and the tips of which bend into pre-existing diapirs (Jackson *et al.* 2008). Increased sedimentation towards the toe of the fold thrust belt caused pinch-out of the detachment, causing grounding between competent layers. This is inferred to be the cause for landward propagation of compression, which eventually caused inversion structures to form in the previously extensional extent of the basin (Jackson *et al.* 2008).

ANGOLAN MARGIN – KWANZA BASIN

The Kwanza Basin in Angola, south-western Africa, underwent three stages of deformation, all with associated salt detachment tectonics. The Kwanza Basin is divided up into an onshore and offshore region, the Inner and Outer, respectively (Hudec & Jackson 2004). The detachment lithology is the Aptian salt or ‘Massive Salt’ (Duval *et al.* 1992). Initially, the detachment horizons in this basin were separated by a high in the centre of the basement (Hudec & Jackson 2004). The Outer Kwanza Basin contains a very thick seaward dipping detachment with an up dip extensional regime and a down-dip compressional regime (Hudec & Jackson 2004).

Similar to the Astrid thrust belt, the ‘trigger’ in the Kwanza Basin was uplift, until increased sedimentation into the toe of the basin caused buttressing of salt nappes and resulted in pinch out of the detachment (Hudec & Jackson 2004). This concentrated compression up dip of the pinch-out forming large-scale fold and thrust belts, a thickened salt plateau and folded and thrusted salt diapirs (Hudec & Jackson 2004). Broad, open, short wavelength folds occur above salt nappes and record no strong vergence in any orientation (Hudec & Jackson 2004).

In summary, both of these regions have oceanward dipping salt detachment layers in a passive margin setting and they have the same tectonic trigger (Morley *et al.* 2011). However, they do not express similar structural geometries. Therefore, the difference must be heterogeneities in the detachment zone. For example, the thickness of the major detachment layer was different for each case study. This project aims to verify if variables, such as changes in the thickness and detachment proximity, are controlling structural styles of overlying rock packages that form fold and thrust belts.

METHODS

Both seismic and field data were utilised to complete this project. Seismic interpretation was undertaken from multiple surveys in the Amadeus Basin using the SMT Kingdom Seismic interpretation Suite 8.6. The main focus was on the structural geometry of horizons and how they relate to each other and the thickness of salt beneath, if applicable. The seismic data contained minimal survey details, hence, only the line name, shot count and record length could be recorded. They can be found in Appendix A.

Fieldwork was conducted to gain structural and sedimentary data along three north-south trending transects. Three cross sections were constructed using apparent dips from direct bedding readings in the field. Fracture data has been manipulated into paleo-stress directions. Methods for calculating paleo-stress orientations, aspect ratios and shortening can be found in their relative sections.

RESULTS

Structural geometries have been documented from seismic and field data, and from these, folding, faulting, aspect ratios and shortening have been observed or calculated.

Structural Interpretation of Seismic

Multiple seismic surveys across the Amadeus Basin have been studied (Figure 7a). The sections were displayed in two-way time and therefore may not display true geometries. However, their relationships to one another were the focus of this study, therefore absolute scale is not necessary. Features that were considered important consisted of the large scale geometry of sub-surface horizons, amplitudes and wavelengths of antiforms and synforms, and the occurrence and nature of large faults. Very few east-west trending lines were used as they did not present many structures. All seismic lines were viewed with a horizontal scale of 1:50000 and a vertical scale of 5 cm/s.

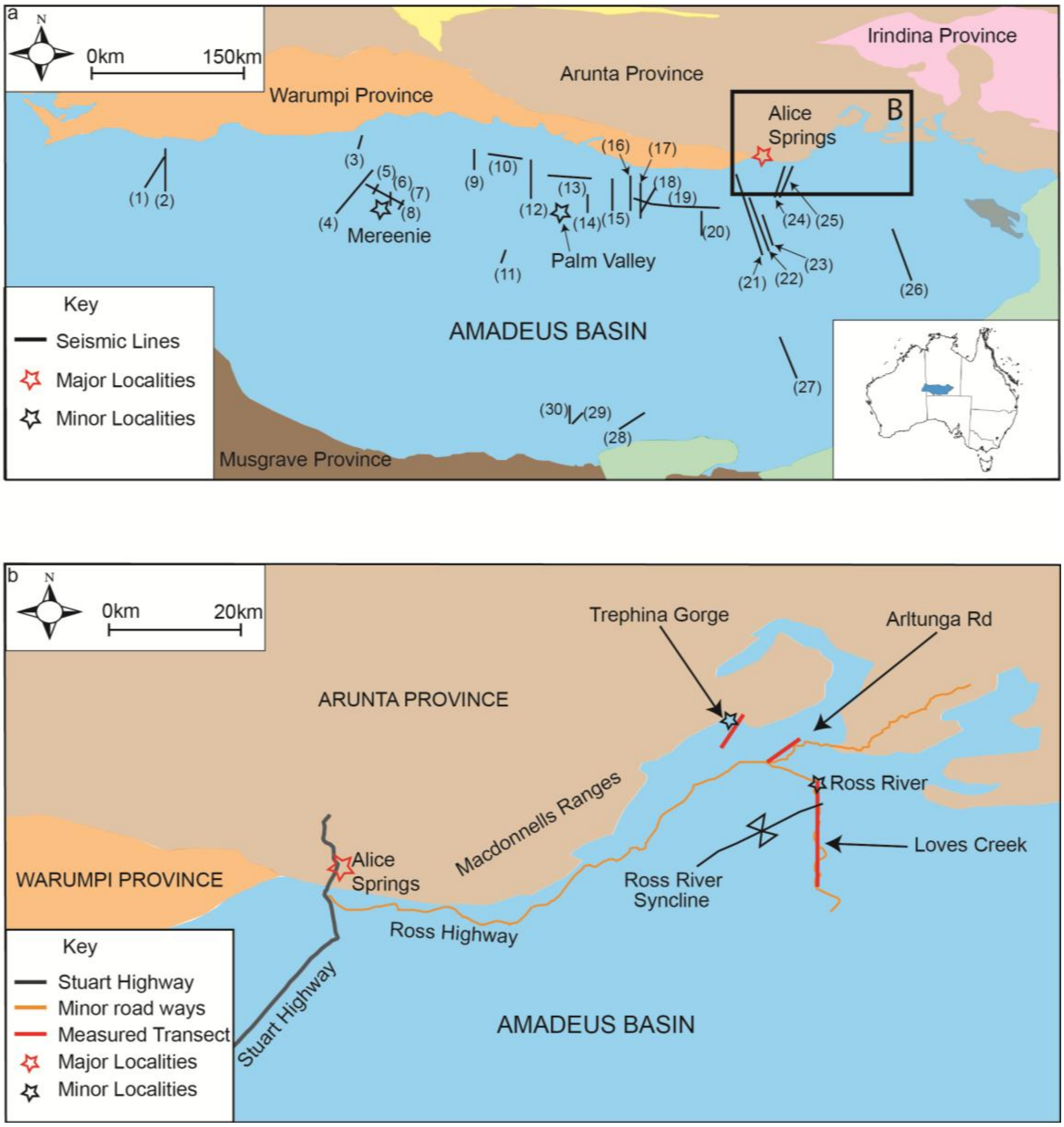

Figure 7. a) Map showing the regional extent of the Amadeus Basin and surrounding provinces. Seismic lines that were used in this study have been outlined. (1) 0-7, (2) P81-J14, (3) M87-TA01, (4) P82-GE41, (5) M83-13, (6) M83-13, (7) M82-10, (8) M82-11, (9) P81-U4, (10) p83-HJ1, (11) I99A-16, (12) 2-5, (13) 2-A, (14) M94-PV040R, (15) 2-1, (16) 3-5, (17) 3-4, (18) 73-3-3.6, (19) 73-3-AEX, (20) 73-3-2.3, (21) 3-1, (22) P80-11, (23) 3-2XDX, (24) P80-2, (25) P80-4, (26) MCF81-07, (27) DH91-2N, (28) 82-01, (29) MR89-102, (30) 82-06 b) Location of fieldwork. Structural data was observed and measured along three transects.

Fieldwork

Fieldwork was conducted to obtain structural and sedimentary data along transects with GPS coordinates (Appendix B). As the Bitter Springs Formation contains evaporite horizons that are inferred to have acted as a detachment, it was important to study areas that were stratigraphically above, below and in this formation. Three north-south or northeast-southwest trending transects were completed and bedding and fracture measurements have allowed for the construction of three two-dimensional cross-sections stereonets, stereonets and paleo-stress orientations. They have been differentiated such that they can be related to their proximity to the detachment horizon.

BEDDING AND FRACTURE DATA

Dip and dip direction data of 241 bedding planes, 91 fracture planes and 24 fault planes were recorded in the Amadeus Basin (Figure 8). These areas have been classified into either being stratigraphically above the Bitter Springs Formation (Julie Formation to Pacoota Sandstone), in the Bitter Springs Formation, or stratigraphically below the Bitter Springs Formation (Heavitree Quartzite) (Figure 3).

Bedding

Density contouring in these stereonets illustrates the low variance of data both above and below the Bitter Springs Formation (Figure 8). The bedding planes have similar orientations, with the mean dip/ dip direction of Loves Creek being 33/190, and 22/120 in Trephina Gorge. Bedding planes within the Bitter Springs Formation contain populations of data points that match both of these mean values. However, data express other populations in many other orientations as well (Figure 8).

The mean dip/dip direction of the Bitter Springs Formation is 39/351. The percentage of data that is close to this, however, is only 3.9%. An average dip of 39˚ can be seen to populate dip directions of 030 NE, 300 NW, 160 SE and 220 SW.

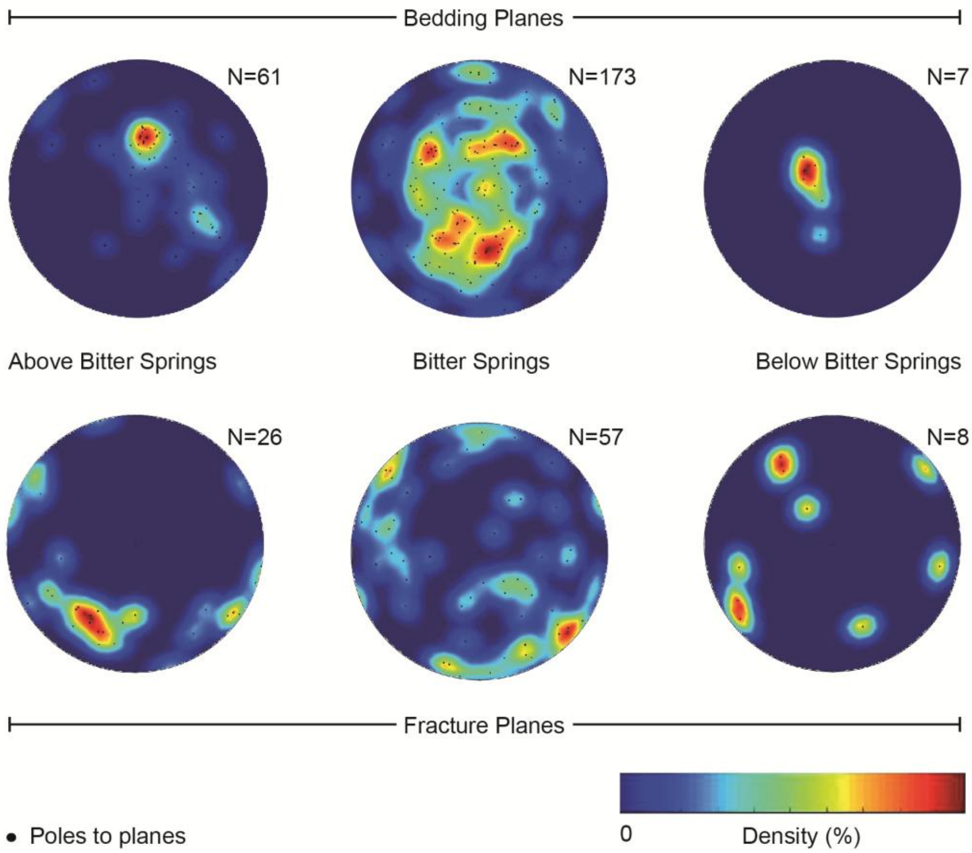

Figure 8. Equal-area, lower hemisphere stereonets constructed from structural field data in the Amadeus Basin. The scatter of orientations of bedding planes can be seen to dramatically increase in the Bitter Springs Formation.

Fractures

Fracture planes were seen and measured along all transects. Descriptions of their orientations are presented. Conjugate fracture sets, where found, have been utilised to derive paleo-stress orientations and consequently paleo-stress regimes. In Loves Creek (Julie Formation to Pacoota Sandstone) (Figure 3), fracture planes are generally oriented steeply to the northeast. These fractures were not cemented and in some cases appeared as conjugate pairs.

In the Bitter Springs Formation, fracture orientations maintain a consistent steep dip. However, the dip direction is highly scattered. The mean dip/dip direction is 83/313.

There appears to be no similarity in populations between this area and the fractures at Loves Creek. Fractures in the Bitter Springs were heavily cemented by calcite (Figure 9a). Cross-cutting relationships were seen in the field and have revealed that a fracture with an orientation of 80/018 is offset by a younger fracture oriented at 78/130. This orientation is very close to the mean, suggesting that most measured fractures were young.

Stratigraphically below the Bitter Springs Formation, in the Heavitree Quartzite, seven fracture plane measurements reveal that there are no similarities between these fracture orientations and the areas that are stratigraphically above. Fractures in the Heavitree Quartzite were silica cemented, and tensile fractures were filed with quartz (Figure 9b).

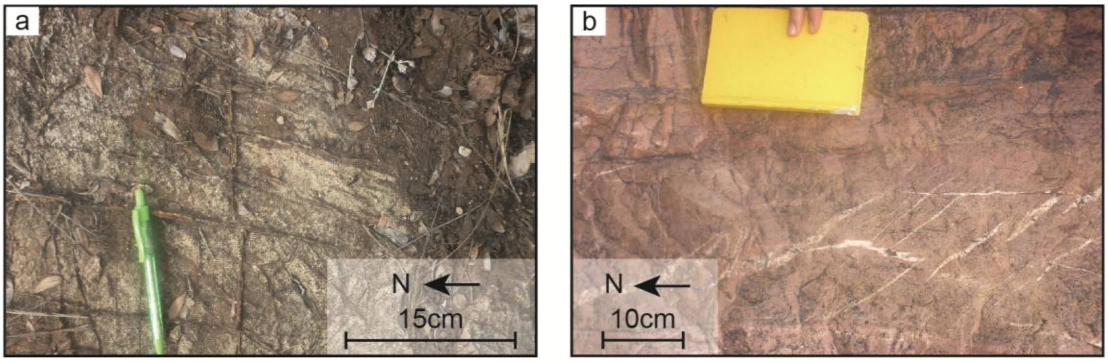

Figure 9. Different types of fractures in the Amadeus Basin. a) Calcite veins in the Bitter Springs Formation. Cross cutting relationships reveal that the E-W vein in this photo has been displaced by left-lateral (sinistral) movement. It is therefore older than the N-S vein. b) precipitation in tensile veins in the Heavitree Quartzite.

Paleo-stress

The orientations of conjugate fractures in outcrop were measured and manipulated on stereonets to give insight into what the stress regime was at the time of their formation. The stress regimes are defined by Anderson 1951, and described in terms of the orientation of the maximum, intermediate, and minimum principle stresses (σ_1, σ_2, σ_3, respectively) (Roering 1968) (Figure10).

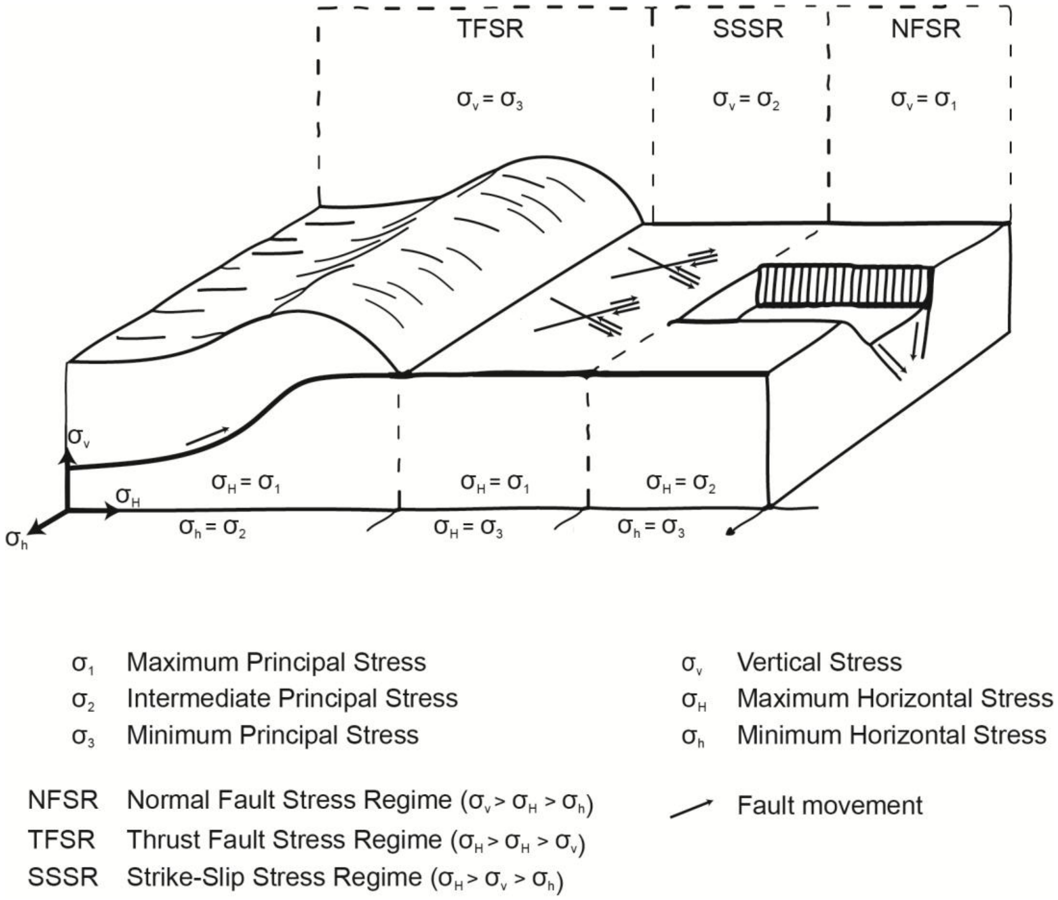

Figure 10. Schematic block diagram illustrating the relative arrangement of principal stresses required to produce a certain stress regime (Anderson 1951). Adapted from Sassi & Faure 1996.

These principal stress directions can be inferred from conjugate fractures. Corrections for bedding planes were not performed, as conjugate fracture sets are inferred to have formed simultaneously with folding (Figure 11c).

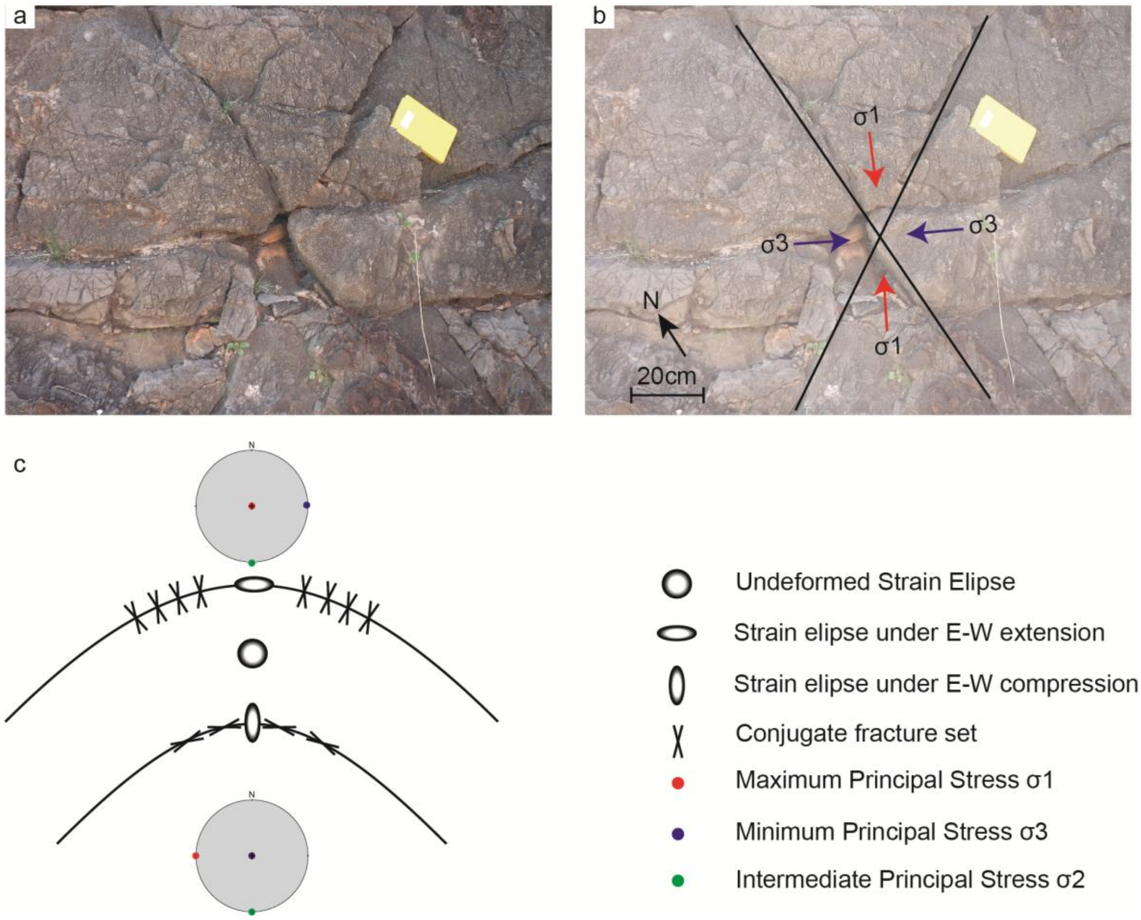

Figure 11. a) Photo 47 Bitter Springs Formation with conjugate fractures. b) Interpretation overlay, with implications of stress directions for conjugate fractures to form. c) Schematic diagram of how conjugate fractures form simultaneously with folding- extension in the outer arc, no strain in the centre, and compression in the inner arc. Stereonets show ideal stress regime (Anderson 1964).

Paleo-stresses are projected on stereonets and are illustrated on the cross sections (Figure 12, 13, 14).

Loves Creek conjugate fractures indicate that during the time they were formed, σ_1 was E-W, σ_2 was N-S and σ_3 was near vertical (Figure 12). This indicates a pure strike-slip stress regime(Anderson 1951).

Along the Arltunga Road Section, σ_1 is vertical in the southwest, indicating a normal stress regime, with σ_3 trending horizontally at 140 SE. The stress regime then appears to change to strike-slip to the northeast, where σ_1 becomes more horizontal and trending 275 W. The third set of paleo-stress data expresses a strike-slip regime, however the maximum principal stress is now trending north-south (010 N) (Figure 13).

Paleo-stress was only obtained in the north-western end of the Trephina Gorge transect (Figure 14). The dip directions of σ_1, σ_2 and σ_3 are practically identical, the dip of σ_1 steepens to the northeast. These measurements infer a strike-slip stress regime, with compression orientated to north-south.

TWO DIMENSIONAL CROSS-SECTIONS

Three two-dimensional (2D) cross sections were constructed from field data, their geographic locations can be seen in Figure 7b.

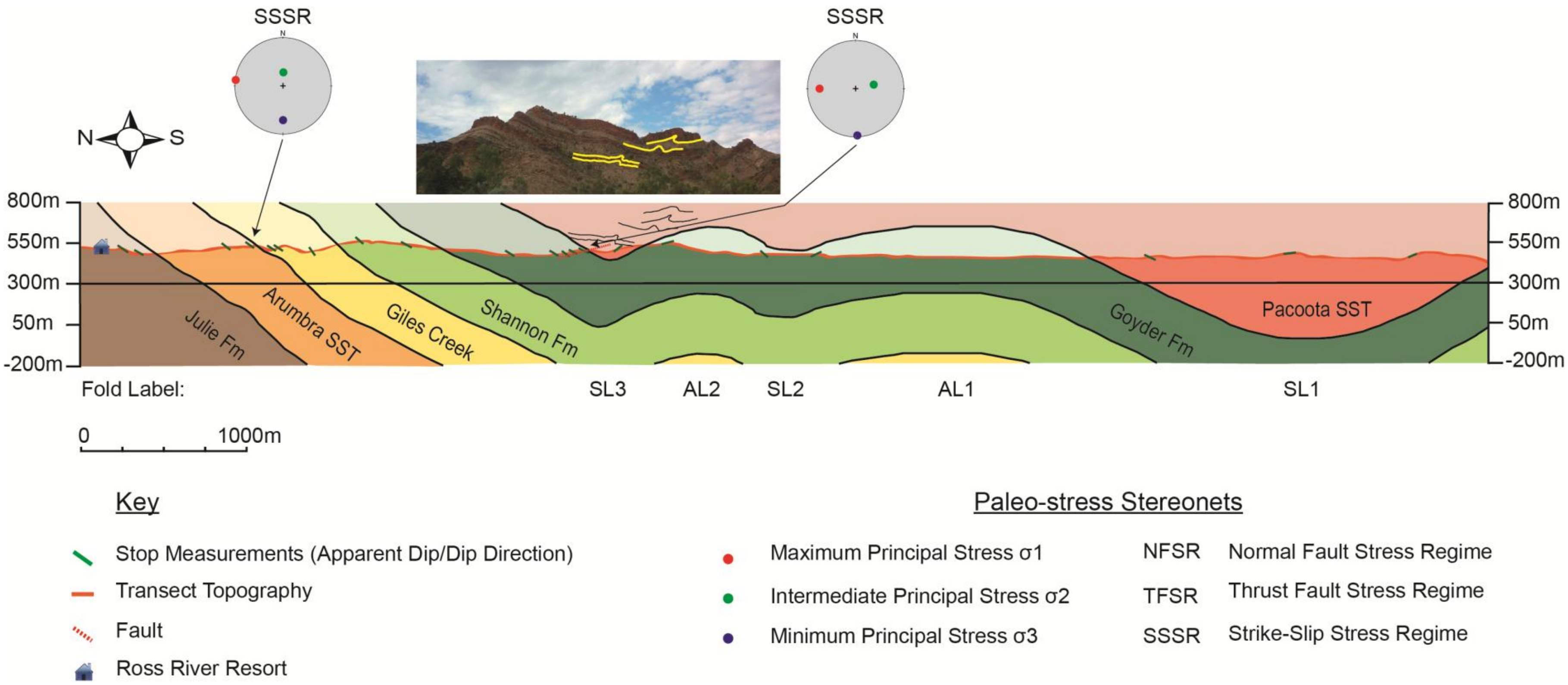

Figure 12. Loves Creek Transect. Regional cross section through Loves Creek. Apparent dips were calculated using trigonometry for a north-south transect line with a 001 degrees section azimuth. The cross section illustrates the relatively simple structure of formations that overly the detachment horizons in the Bitter Springs Formation (Figure 3). The orientation of horizontal paleo-stresses remain constant, with the maximum horizontal stress trending east-west. The photo inlay represents some smaller fold structures see within these units.

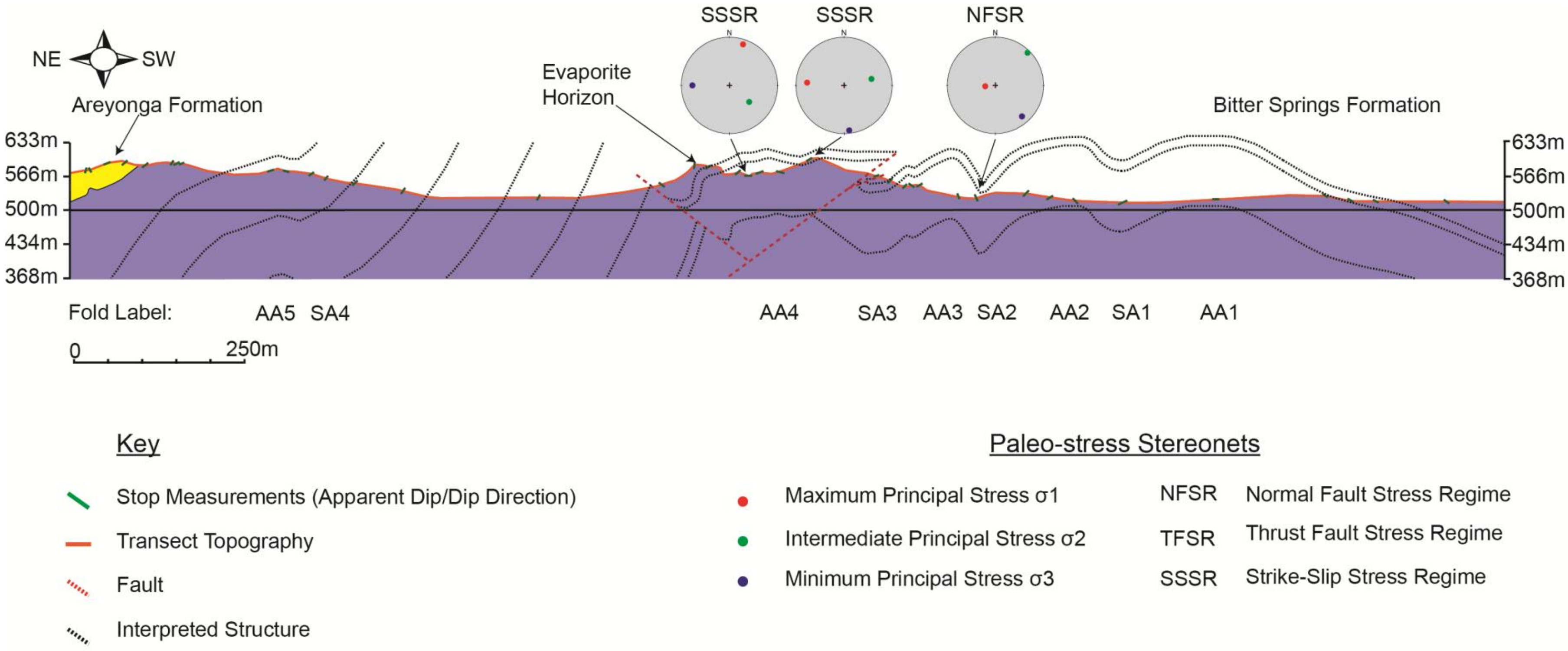

Figure 13. Arltunga Road Transect. Two-dimensional cross section along a northeast-southwest trending transect line. Apparent dips were calculated with trigonometry using a section azimuth of 053 degrees. North-south compression combined with somewhat ductile dolomite leads to a complexly folded and apparently thick package of rocks.

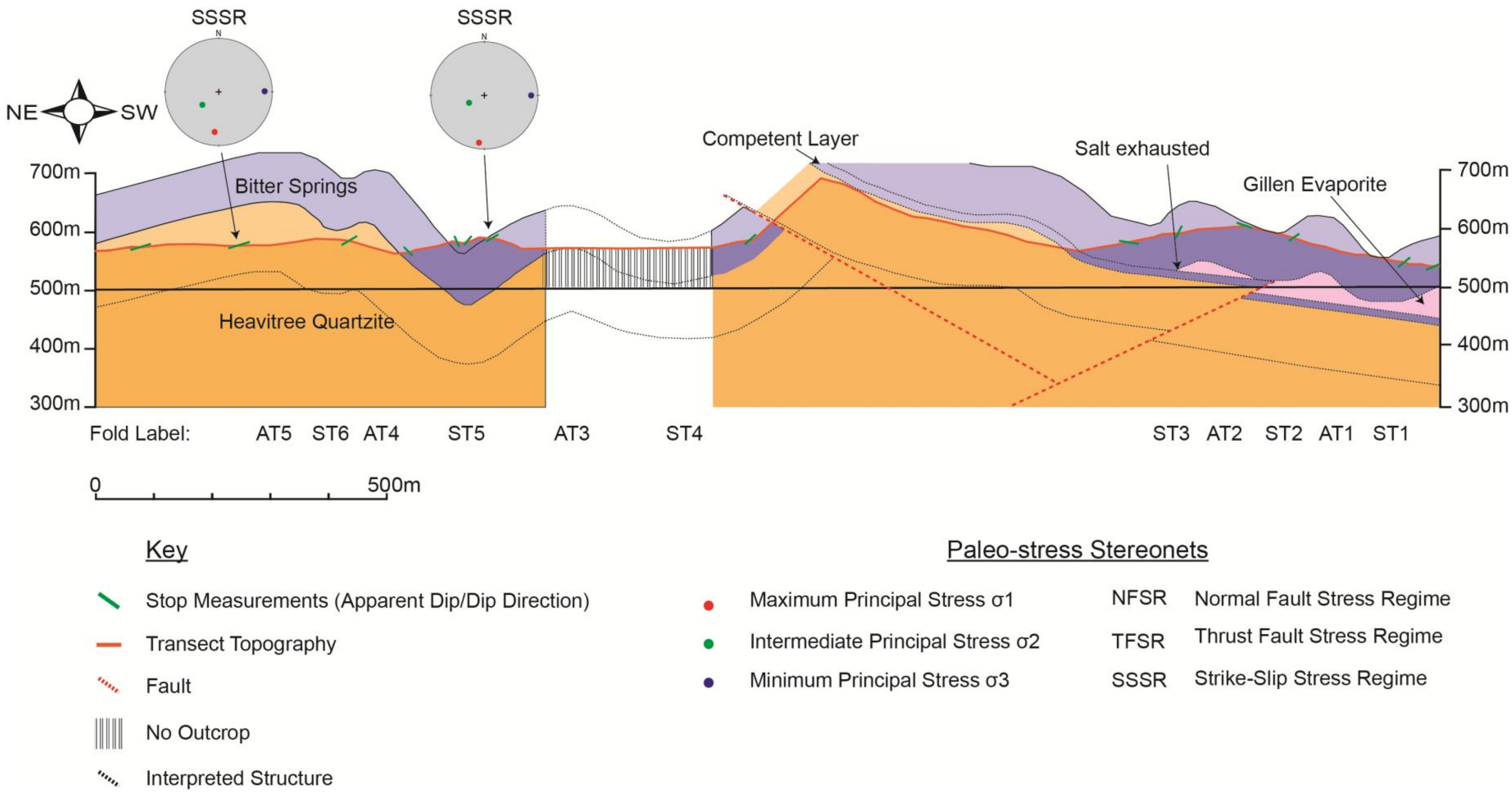

Figure 14. Trephina Gorge Transect. Two-dimensional cross section along a northeast-southwest trending transect line with a section azimuth of 053 degrees. The section shows a back-thrust with a great enough vertical throw to exhume the Heavitree Quartzite, which has been made possible by grounding due to a lack of salt between competent layers in the Bitter Springs Formation and Heavitree Quartzite – see Discussion.

Fold geometries in the Amadeus Basin from seismic and field data

FOLD GEOMETRIES IN SEISMIC DATA

The sub-surface of the Amadeus Basin is populated by a number of rounded folds that range from tight to open, symmetric and asymmetric, and can vary considerably in size from 5-20 km half wavelengths ($\lambda/2$). The half wavelength is defined as the length between two points of inflection on either sides of a fold. Layers appear to keep constant thicknesses around fold hinges and are, therefore, classified as 1B folds (Ramsay 1967) (Figure 15b). In general, antiforms have smaller half wavelengths than the synforms, and both express little to no vergence.

Salt-cored antiforms are rare in the seismic, however, were key in understanding the relationship between fold geometry and detachment thickness. The following table summarises the fold geometries, aspect ratios and shortening calculations (Table 1).

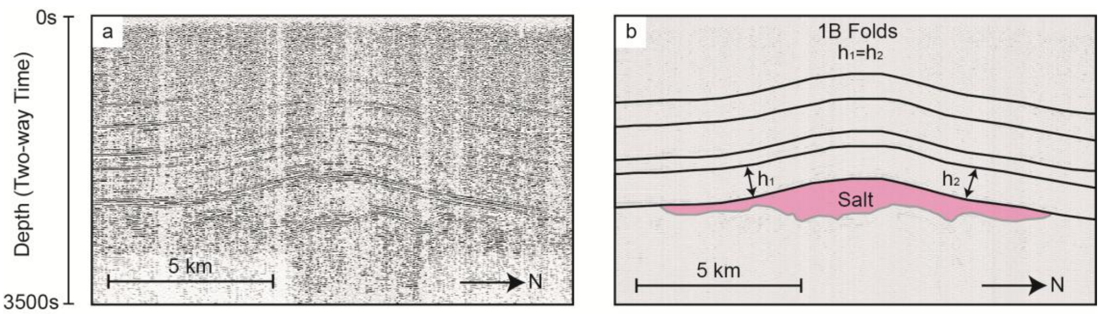

Figure 15. a) Seismic line M94-PV04R with the structural interpretation (b) illustrating 1B fold style (Ramsay 1967). This interpretation also illustrates the nature of salt in the core of an antiform.

Table 1. Summarised fold properties, fold shapes, aspect ratios and shortening calculations from seismic lines containing salt-cored antiforms in the Amadeus Basin.

Seismic line	2-5	M94-PV04R	3-5	3-4	73-3-3.6	P80-11
Above/in/ below BSF	Above	Above	Above	Above	Above	Above
Antiform/ Synfrom/ both	Antiform	Antiform	Monocline	Antiform	Antiform	Both
Class (Ramsay 1967)	1B	1B	1B	1B	1B	1B
Fold symmetry	Symmetric	Symmetric	Symmetric	Symmetric	Symmetric	Symmetric
Shape of fold limbs	Curved	Curved	Curved	Curved	Curved	Curved
Shape of fold hinge	Round	Round	Round	Round	Round	Round
½ wavelength (cm)	12.59	12.76	5.43	6.73	9.50	6.80
Arc Length (cm) north	7.01	21.82	5.70	7.86	9.40	6.90
Amplitude (cm)	0.75	0.75	0.55	1.26	1.31	0.48
Aspect ratio (wavelength)	0.06	0.06	0.10	0.19	0.14	0.07
Aspect ratio (arc length)	0.11	0.03	0.10	0.16	0.14	0.07
Approximate distance from salt	1.58	4.11	2.42	2.82	3.25	1.27
Thickness of salt (cm)	0.45	1.59	1.15	1.31	1.34	0.34
Un-shortened length L_0	26.01	21.61	24.8	27.5	23.96	28.03
Shortened length L_1	26.21	21.82	25.25	28.29	24.66	28.23
Shortening (%)	0.76	0.96	1.78	2.79	2.84	0.71

In the northwest of the basin, seismic line 0-7 (Figure 7a, (1)) images a large ($\lambda/2$ =10 km), symmetric, angular antiform, which is seen between even larger ($\lambda/2$ =13 km), open and more broad synforms (Figure 16b). Heading east, the folds verge south, however the overall geometries appear to be constant.

In the seismic lines from the Mereenie area (Figure 7a, (4)-(8)), asymmetric antiform-synform pairs are seen with a slight northward vergence (Figure 16d). Antiformal wavelengths have decreased ($\lambda/2$ =7 km).

In-between the Mereenie and Palm Valley region, seismic line P81-U4 (Figure 7a, (9)) shows a north-dipping thrust fault with a fault-bend fold forming as a result. The displacement o this thrust fault is at least 1 km.

Moving further to the Palm Valley region (Figure 7a), overall geometries of folds remain consistent with other folds in the basin, however, now express no vergence as seen in seismic line M94-PV40R (Figure 15b). This antiform is broad, shallow, symmetric and salt cored. No complete synforms were imaged in surveys from this area of the basin. This is inferred to be a result of large wavelengths and consequently the extent of seismic does not cover them.

The north-eastern margin of the basin, south of Alice Springs, contains a large amplitude synform with a blind thrust that dips north, forming asymmetric forced-folds with a southward vergence (Figure 16h).

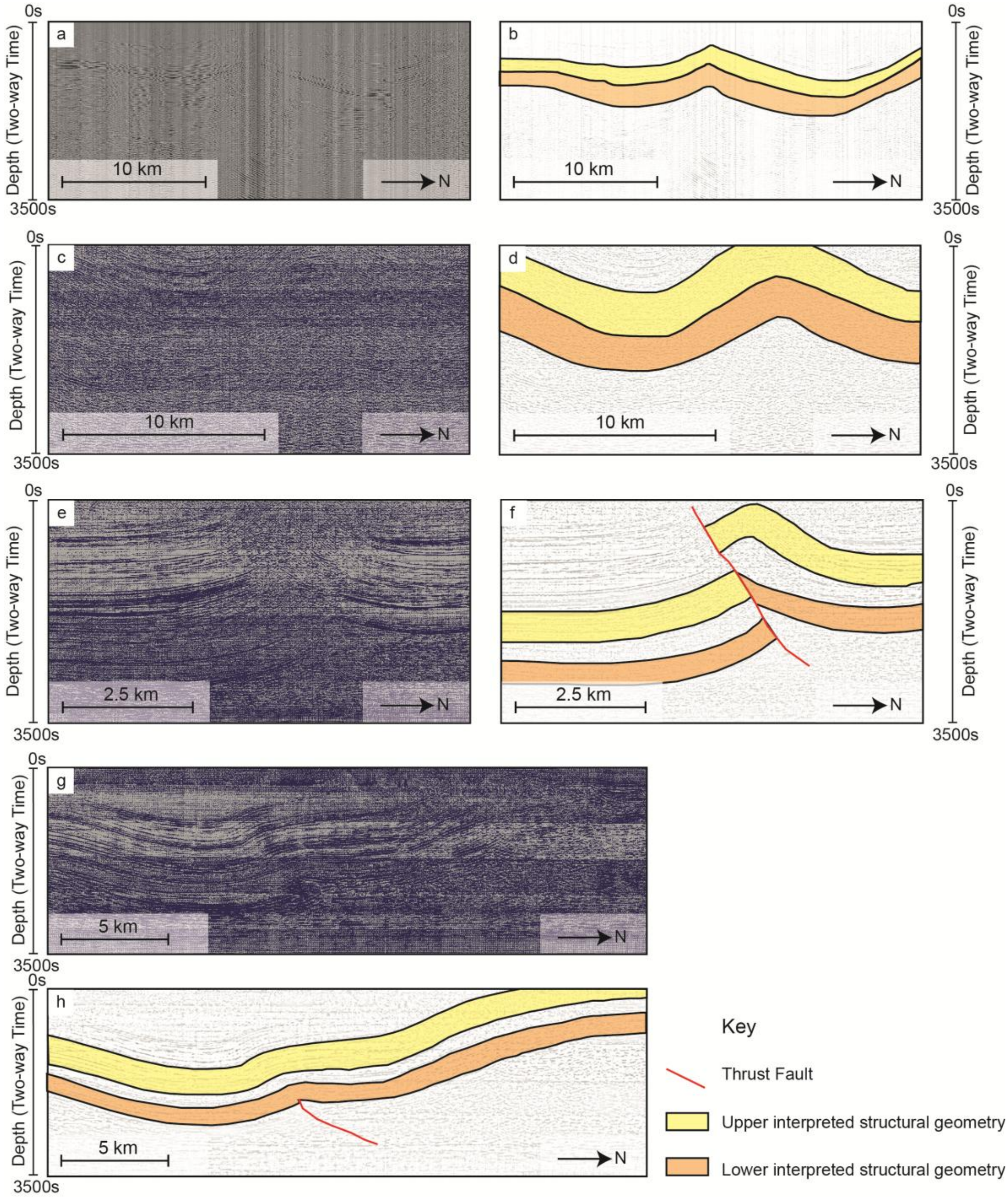

Figure 16. Seismic lines from the Amadeus Basin with interpreted structural geometry they illustrate. a) Line 0-7. b) Interpreted section showing angular antiformal hinge surrounded by larger wavelength synforms. c) Line P82-GE41. d) Interpreted section showing a large amplitude antiform-synform pair with a very slight southward vergence. e) Line P81-U4. f) Interpreted structure showing a large north-dipping thrust fault that cuts through the hinge of an antiform, forming a fault-bend fold on the hanging wall. g) Line P80-2. h) Interpreted structure showing a force-fold antiform on the northern limb of a synform with large wavelength ~ 15 – 20 km. A blind thrust is responsible for the antiform.

FOLD GEOMETRIES IN CROSS-SECTIONS

The construction of cross-sections has outlined the significant amount of folding that has occurred in the Amadeus Basin. Cross-section geometries were interpreted with due consideration of smaller scale structures that were observed in the field. Therefore, smaller scale geometries are not presented.

Below, a south to north description for the Loves Creek transect, and southwest-northeast description for the remaining transects are presented below. For full GPS locations and full transect details, refer to Appendix B.

Loves Creek Transect - Figure 12

Starting at the southern end of the transect, a broad, open synform (SL1) has a symmetric geometry and has a rounded hinge and limbs (Figure 12). Once the northern limb is crossed, outcrop disappears, marking the hinge of a now eroded antiform (AL1) (Figure 12). Outcrop reappears in the hinge of the synform SL2, followed by a slightly northward verging antiform with similar geometry and amplitude (AL2) (Figure 12). The Ross River Synform, here labelled SL3, has a smaller inter-limb angle causing the reappearance of the Pacoota Sandstone in the hinge.

Heading further north, beds maintain a constant moderate-steep dip to the south. Planar cross bedding was common in these units and provided a younging direction that indicated these beds were the right way up.

Arltunga Road Transect - Figure 13

The south-west end of this section expresses a relatively simple overall geometry compared to the remaining section. Dolomite beds have a moderate dip to the south-west, where folding and faulting is present at field scale (20 cm amplitudes). Thrust slip surfaces dip west-southwest with an unknown displacement, as in most cases a bedding plane was the slip plane.

Moving further northeast along the section, the regional dip becomes horizontal as a broad, open antiform is crossed (AA1). Following this, an open synform (SA1) with a slightly smaller inter-limb angle and slightly northward verging antiform (AA2) is seen, before an angular, tight, symmetric synform (SA2) and antiform (AA3) pair is seen.

AA3 antiform is a smaller antiform-synform pair with a similar geometry. At the field scale, a number of smaller folds are seen with upright to shallow axial planes and variable plunge and plunge directions.

Two forward-thrust faults dip northeast and offset layers in the Bitter Springs Formation, as well as causing changes in topography. The south-western most thrust is depicted as a splay with minimal vertical throw compared to the larger thrust (Figure 13).

In between the fore-thrusts and back-thrust, a pop-up structure is observed (Figure 13). It consists of layers in the Bitter Springs Formation which demonstrate a number of small ($\lambda/2$ = 30-40m), open, broad antiforms and synforms. These folds have been grouped into AA4 as a large, north-verging, asymmetric antiform makes up the larger scale geometry. A large back-thrust has sheared off the north-eastern limb of a synform.

On the northern limb the of the back-thrust, a very fine grained smooth rock with no identifiable bedding plane was observed. This is interpreted to be an evaporite horizon from the lower Gillen Member (Figure 17). The rock exhibits very different weathering patterns compared to surrounding competent layers of dolomite, where no plane of weakness is exploited. A strange laminar texture on the surface gives the appearance of bedding.

Figure 17. Paleo-detachment layer in outcrop along the Arltunga Road transect (Figure 7b). This unusual lithology was encountered between competent layers of dolomite in the Bitter Springs Formation. The rock is very fine grained, smooth, and has a very different appearance to the surrounding rocks.

Moving further north-east, outcrop was scarce. It was eventually found, however, that beds were dipping north-east. Synform SA4 and antiform AA5 make up a large monocline before the overlying Areyonga Formation is encountered (Figure 13).

Trephina Gorge - Figure 14

The south-western end of the transect consists of asymmetric folding of the Bitter Springs Formation (Figure 14). Antiforms AT1 and AT2 express a slight vergence to the north, and have half wavelengths of 125 m. Synforms between these antiforms (ST1, ST2, ST3) express similar inter-limb angles, however, have larger half wavelengths ($\lambda/2 = 140$ m).

A topographical high at 700 m above sea-level is composed of the Heavitree Quartzite and marks the bluff of Trephina Gorge (Figure 14). This is interpreted to be the result of a large back-thrust. On the north-eastern slope of the bluff, beds of the Bitter Springs Formation dip northeast and mark the southwest limb of synform ST4.

A period of no outcrop follows ST4, however, an antiform has been interpreted, as the next outcrop revealed beds in the Bitter Springs Formation that dip north. The next fold, ST5, is symmetric synform with an angular inner-arc. Following these are two low wavelength folds, AT4 and ST6, followed by an asymmetric, broad antiform with a south-west vergence.

Table 2. Summarised fold properties, dimensions and fold shapes along Loves Creek and Arltunga Road Transects.

Transect	Cross-section code	Oldest formation (Figure 2)	Youngest formation (Figure 2)	Faults present	½ wavelength (m)	Arc Length (m) north	Amplitude (m)	Aspect ratio (wavelength)	Aspect ratio (arc length)	Class (Ramsay 1967)	Fold symmetry	Shape of fold limbs	Shape of fold hinge
Loves Creek	SL1	Goyder	Pacoota	-	1983.6	2131.148	327.9	0.165	0.154	1B	Symmetric	Curved	Round
	AL1	Goyder	Goyder	-	1901.6	2000.000	180.3	0.095	0.090	1B	Symmetric	Curved	Round
	SL2	Goyder	Goyder	-	393.4	409.836	49.2	0.125	0.120	1B	Symmetric	Curved	Round
	AL2	Goyder	Goyder	-	688.5	786.885	114.8	0.167	0.146	1B	Asymmetric	Curved	Round
	SL3	Julie	Pacoota	Small thrust dipping north	508.2	639.344	147.5	0.290	0.231	1B	Symmetric	Curved	Round
Arltunga Road	AA1	Bitter Springs	Bitter Springs	-	202.5	221.500	31.6	0.156	0.143	1B	Symmetric	Curved	Round
	SA1	Bitter Springs	Bitter Springs	-	75.9	94.900	15.8	0.208	0.166	1B	Symmetric	Curved	Round
	AA2	Bitter Springs	Bitter Springs	-	126.6	151.900	22.2	0.175	0.146	1B	Asymmetric	Curved	Round
	SA2	Bitter Springs	Bitter Springs	-	60.1	120.300	31.6	0.526	0.263	1B	Symmetric	Curved	Angular
	AA3	Bitter Springs	Bitter Springs	-	66.5	88.600	22.2	0.334	0.251	1B	Asymmetric	Curved	Round
	AA4	Bitter Springs	Bitter Springs	Bound by north-dipping fore-thrust and south-dipping back-thrust	123.4	152.000	19.0	0.154	0.125	1B	Asymmetric	Curved	Round

Table 3. Summarised fold properties, dimensions and fold shapes along Trephina Gorge Transect.

Transect	Cross-section code	Oldest formation (Figure 2)	Youngest formation (Figure 2)	Faults presen	½ wavelength (m)	Arc Length (m) north	Amplitude (m)	Aspect ratio (wavelength)	Aspect ratio (arc length)	Class (Ramsay 1967)	Fold symmetry	Shape of fold limbs	Shape of fold hinge
Trephina Gorge	ST1	Bitter Springs	Bitter Springs	-	96.2	118.6	32.1	0.334	0.271	1B	Symmetric	Curved	Round
	AT1	Bitter Springs	Bitter Springs	-	102.6	121.8	25.6	0.250	0.210	1B	Asymmetric	Curved	Round
	ST2	Bitter Springs	Bitter Springs	-	109.0	128.2	19.2	0.176	0.150	1B	Asymmetric	Curved	Round
	AT2	Bitter Springs	Bitter Springs	-	115.4	141.0	19.2	0.166	0.136	1B	Asymmetric	Curved	Round
	ST3	Bitter Springs	Bitter Springs	-	125.0	141.0	19.2	0.154	0.136	1B	Asymmetric	Curved	Round
	ST4	Bitter Springs	Bitter Springs	Back-thrust through south-west	221.2	250.0	41.7	0.189	0.167	1B	Symmetric	Curved	Round
	AT3	Bitter Springs	Bitter Springs	-	185.9	198.7	32.1	0.173	0.162	1B	Symmetric	Curved	Round
	ST5	Bitter Springs	Bitter Springs	-	134.6	198.7	54.5	0.405	0.274	1B	Symmetric	Curved	Round
	AT4	Heavitree	Bitter Springs	-	134.6	147.4	32.1	0.238	0.218	1B	Asymmetric	Curved	Round
	ST6	Heavitree	Heavitree	-	54.5	64.1	16.0	0.294	0.250	1B	Asymmetric	Curved	Round
	AT5	Heavitree	Heavitree	-	189.1	205.1	22.4	0.118	0.109	1B	Asymmetric	Curved	Round

Aspect ratio analysis of folds in the Amadeus Basin

The aspect ratio of a fold relates its amplitude to its wavelength or arc length. An ideal buckle fold will have an amplitude that is equal to half the wavelength (or arc length), yielding an aspect ratio equal to 1.

$$\boldsymbol{R} = \frac{\mathbf{A}}{\tfrac{1}{2}\boldsymbol{\lambda}\ \mathbf{or}\ \boldsymbol{l}}$$

$\boldsymbol{R}$ = Aspect Ratio
A = Fold amplitude
$\boldsymbol{\lambda}$ = Wavelength
$\boldsymbol{l}$ = Arc length

As the difference between the numerator and denominator increases, an increase in amplitude or a decrease in wavelength, or both, can be inferred. If they are changing proportionately to each other, the aspect ratio will remain constant.

A perfect buckle fold is not common in nature, thus the aspect ratio of a fold is more useful for comparing to other variables that control folding, which in this study is interpreted to be detachment properties.

Aspect ratios were calculated after taking measurements from antiforms in the seismic and in the cross-sections (Table 1, 2, 3).

ASPECT RATIOS OF FOLDS IN SEISMIC

Sub-surface images of salt cored detachment folds were rare. Six were chosen and aspect ratios have been calculated and plotted against both detachment proximity and detachment thickness to evaluate the relationship between fold geometry and detachment properties.

Unfortunately, fold dimensions in seismic are all considered relative, as the sections were displayed in time, not depth, hence only the ratios can be compared to other ratios obtained from seismic, not those that are to scale in the cross-sections and field.

As seen in Figures 5b and 16b, the vertical thickness of salt can be interpreted. This has been utilised to compare to the overriding fold geometries (Figures 18, 19). The thickness of salt on this graph is an arbitrary value, as the vertical scale is not in metres, but seconds. Therefore the results are referred to as the ‘seismic salt thickness’, and appear as integers, where a higher number represents a thicker layer of salt.

Salt Thickness

The relationship between fold geometry and salt thickness can be seen on Figure 18. Although the density of data is low, the trend seen illustrates the fact that an increase in the thickness of salt beneath an antiform will decrease the wavelength amplitude and arc length.

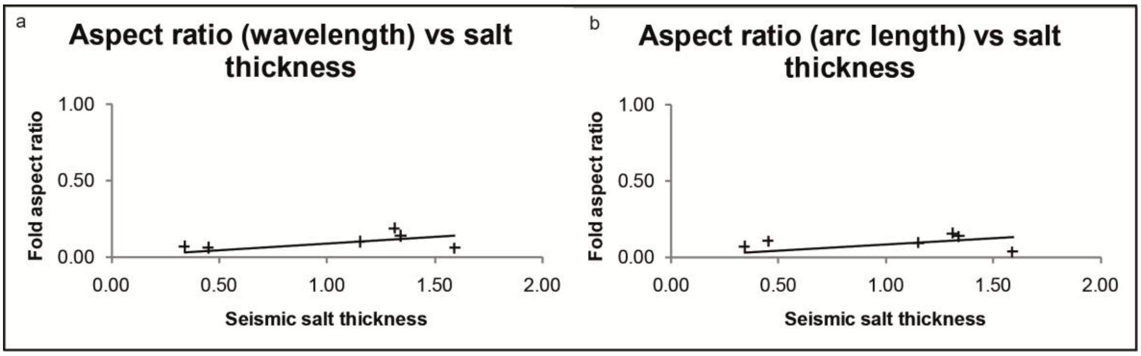

Figure 18. The effect of salt thickness on fold geometry derived from seismic. a) Scatter plot showing the linear relationship between the fold geometry of an antiform and the thickness of salt in its core. The aspect ratio appears to increase as the thickness of salt increases. b) Scatter plot showing the linear relationship between the breadth of an antiform and the thickness of salt in its core. The arc length appears to decrease (as it is inversely proportional to the aspect ratio) as the thickness of salt increases. From these graphs it can therefore be assumed that salt thickness has an influence on fold amplitude, wavelength and arc length.

Detachment Proximity

The relationship between how close packages of rocks are to the basal detachment and fold geometry is illustrated on Figure 19. The aspect ratio appears to increase as rocks move away from the detachment. This implies that the overall fold size is decreasing, much like the salt thickness relationship in Figure 18.

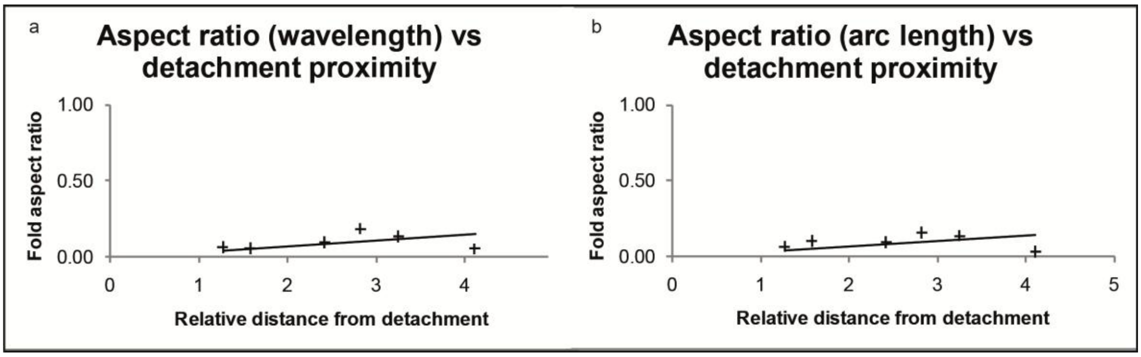

Figure 19. The effect of a detachment layer proximity on fold geometry derived from seismic. a) Scatter plot showing the linear relationship between the fold geometry of an antiform and the proximity of the measured layer to the detachment horizon. The aspect ratio appears to increase as the distance between the measured layer and detachment layer increases. b) Scatter plot showing the linear relationship between the breadth of an antiform and the thickness of salt in its core. The arc length appears to decrease as the thickness of salt increases. From these graphs it can be assumed that detachment proximity has an influence on the amplitude, wavelength and arc length.

ASPECT RATIOS OF FOLDS IN CROSS-SECTIONS

Both antiformal and synformal geometries were measured from cross-sections that were constructed in this study (Figure 12, 13, 14). As appose to the seismic data, cross-sections are to scale, therefore measured fold geometries can be given in units, and aspect ratios will be more accurate.

Unlike the previous section, salt thickness could not be a variable, therefore, detachment proximity was the main focus of this analysis. The detachment layer is inferred to be marked by the presence of the evaporite horizon that was encountered along the Arltunga Road transect (Figure 13, 17). Thus, Trephina Gorge has not been included, as evaporite horizons were not encountered along that transect.

Detachment Proximity

Initial measurements of amplitudes of folds in the cross-sections present strong evidence for the affect of the presence of a detachment on fold geometry. Figure 20 shows the relationship between fold amplitude and detachment proximity. It is evident that the detachment layer greatly decreases the amplitude of folds as it is approached (Figure 20).

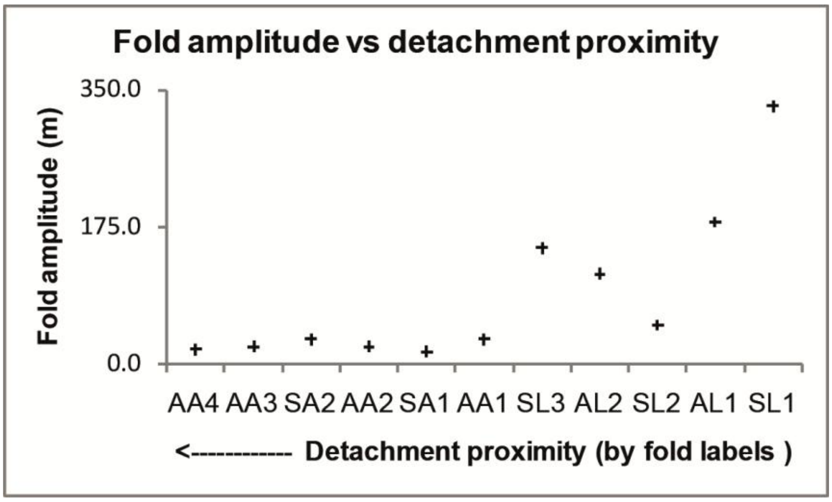

Figure 20. The effect of detachment proximity on amplitudes derived from field data. The x-axis is comprised of fold codes, and can be found on the cross-sections (figure 12, 13). The scatter plot shows the relationship between fold amplitude and detachment proximity from measurements of folds in cross sections. Fold amplitude appears to exponentially decrease as the detachment layer is approached.

Aspect ratios calculated from these folds yield a relationship which is dissimilar to the seismic scatter plots. Figure 21 illustrates the effect of detachment proximity on amplitude, with respect to wavelength and arc length. In this case, aspect ratios are quite scattered, however, overall infer a opposite relationship to the one presented by the seismic data. These scatter plots illustrate an increase in aspect ratio as the distance from the detachment is increased, therefore rocks closer to the detachment layer will have smaller wavelengths and arc lengths (Figure 21).

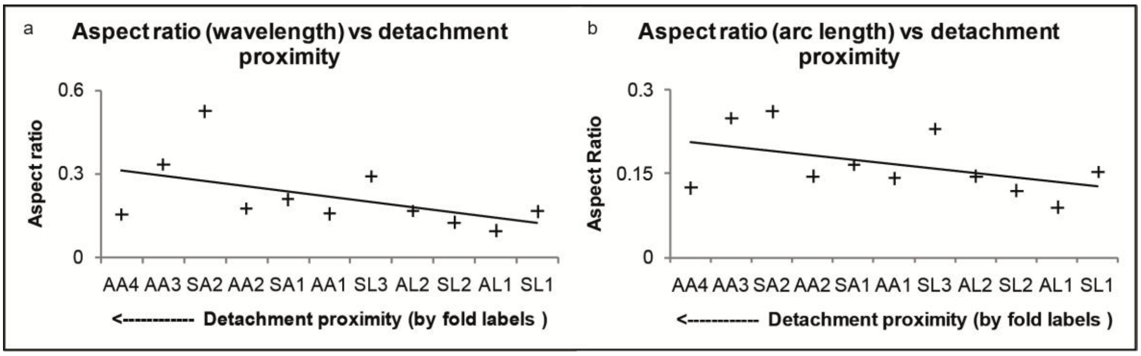

Figure 21. The effect of detachment proximity on fold geometry derived from field data. The x-axis is comprised of fold codes and can be found on the cross-sections (figure 12, 13). a) Scatter plot showing the relationship between fold geometry and detachment proximity. Wavelengths appear to decrease as the distance to detachment is increased. b) Arc length aspect ratios yield a similar relationship to amplitude aspect ratios. Whereby rocks closer to the detachment will have shorter arc lengths.

Shortening estimates from seismic and field data

Calculating the amount of shortening that a package of rocks above a detachment layer may give insight into the influences of the detachment on structural style. An extensional strain equation was used to calculate the amount of shortening:

$$\boldsymbol{e} = \frac{\boldsymbol{L_1} - \boldsymbol{L_0}}{\boldsymbol{L_0}} \times \mathbf{100}\%$$

$\boldsymbol{e}$ = shortening (%)
$\boldsymbol{L_0}$ = initial length
$\boldsymbol{L_1}$ = shortened length (Twiss & Moores 1992)

The result of this equation yields a negative number, as compression results in a negative increase in extension. For this study, negative notation has been removed, as only % shortening is measured. Thus, all values with a higher number correspond to greater amounts of shortening.

Shortening estimates have been derived from salt-cored folds in seismic data (Table 1), as well as folds from cross-sections (Table 2, 3), and field outcrop (Figure 22).

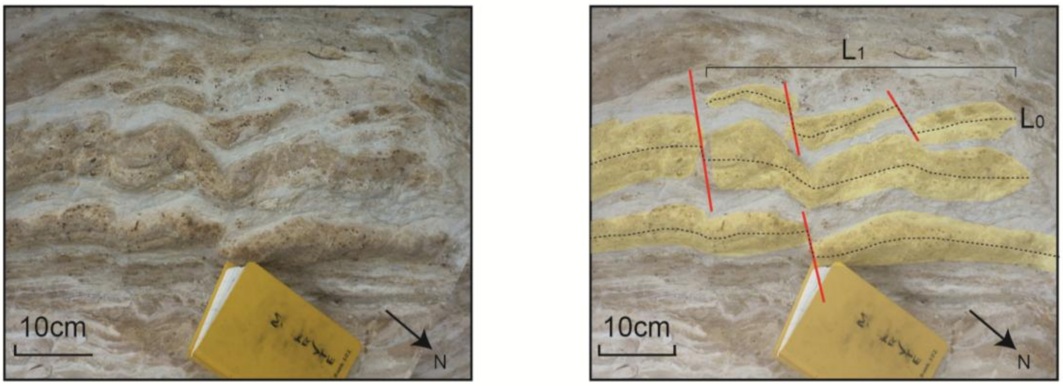

Figure 22. An illustrative method of the process of calculating shortening from field photos. A sequence of rocks will have an initial length, L_0, which can be measured and compared with the shortened length L_1.

SHORTENING ESTIMATES FROM SEISMIC

Shortening estimates have been calculated on 27 seismic sections in packages of rock that lie stratigraphically above the Bitter Springs Formation. They have been compared with each other as well as to the thickness of, and proximity to, the interpreted detachment layer.

Geographical relationships in shortening are illustrated on Figure 23. Shortening calculations have been plotted against their relative seismic line (Figure 7a), which have then been ordered from northwest, to northeast, to south areas of the basin (Figure 23). Shortening amounts in the northwest average at around 8%. Heading east, shortening amounts decreases and continue to fluctuate between 0.05 and 4 % (Figure 23). Seismic line 82-01 marks the beginning of a notable increase in shortening, representing the transition from the northeast area of the basin to the south (Figure 7a).

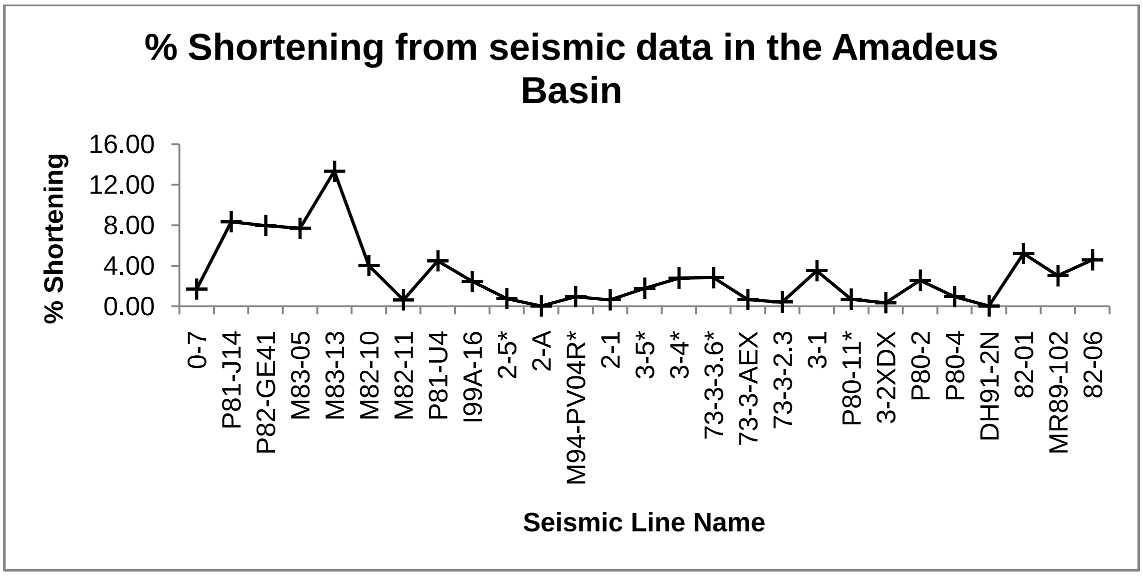

Figure 23. Shortening amounts with respect to the geographical distribution of seismic lines in the Amadeus Basin (7a). Seismic lines are arranged from northwest, to northeast, to central south areas of the Amadeus Basin. Competent layers in the northwest and central north parts of the basin exhibit greater amounts of shortening than other areas of the basin. Seismic lines labelled with (*) represent the presence of salt-cored antiforms.

Salt thickness and detachment proximity

Salt thickness is seen to influence shortening via a linear relationship (Figure 24a). Variations in shortening, however, are only on the scale of 2 - 3 %. Detachment proximity mimics this relationship (Figure 24b).

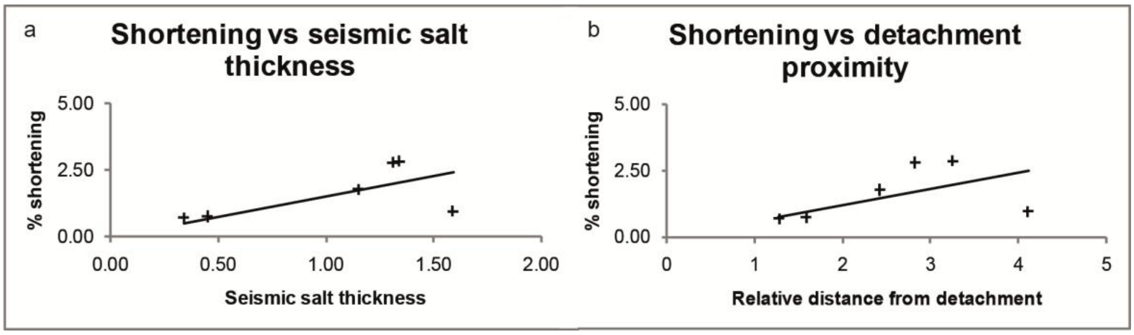

Figure 24. Shortening amounts with respect to salt thickness and proximity from seismic data. a) Scatter plot illustrating the linear relationship between salt thickness and the amount of shortening. A thick layer of salt will cause greater shortening in the overlying layers. b) Scatter plot illustrating the linear relationship between salt proximity and the amount of shortening.

SHORTENING ESTIMATES FROM CROSS-SECTIONS AND FIELD DATA

Extensive folding in the Amadeus Basin has been represented in Figures 12, 13 and 14. With transects above and in the Bitter Springs Formation, shortening estimates could be related to detachment proximity for the same reasons as with aspect ratio analysis.

In this section, shortening estimates from field outcrops have been calculated, and the outcrops location has been measured to the outcropping evaporite horizon along the Arltunga Road transect (Figure 13), to give the lateral distance to the detachment horizon. Note that this is not the vertical distance to detachment, however a strong relationship within 1 km proximity is apparent. Whole section shortening was also calculated, the result reflects the same relationship as field outcrops (Figure 25). As the detachment horizon is approached, shortening amounts increase (Figure 25).

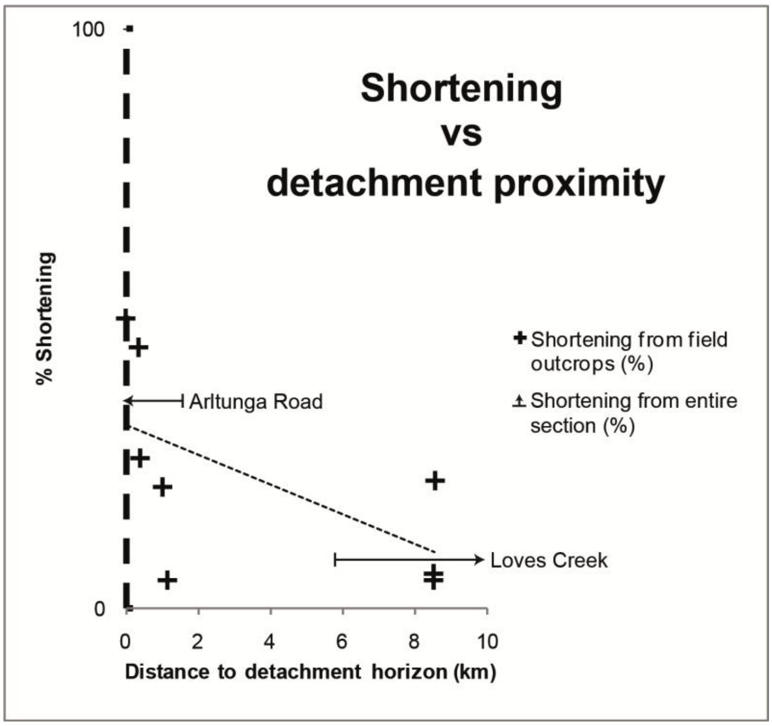

Figure 25. The relation between shortening and distance to detachment from field outcrops. Although there is a large distance gap (6 km), it can be assumed that shortening amounts are not affected by the detachment until 1 km proximity is reached. Section averages of Loves Creek (6 %) and Arltunga Road (37 %) supports the relationship that rocks closer to a detachment layer will express greater amounts of shortening.

DISCUSSION

The Bitter Springs Formation has influenced the present-day geometry of structures in a number of ways since the Late Proterozoic (Flöttmann & Hand 1999). It has done this through its ability to act as a detachment through its incompetent evaporite horizons of the lower Gillen Member (Figure 3) (Wells *et al.* 1970). The presence of this detachment layer alters the structural style of surrounding formations. Certain structural characteristics such as fold geometries can be related to thickness of, or proximity to, the detachment layer.

Detachment proximity

Detachment proximity is inferred to play the major role in a detachments ability to control structural style. Initial field observations and structural measurements have outlined the influence of a detachment layer on the orientation of bedding in the layers above it. Dip/dip direction measurements of bedding planes above and below the Bitter Springs Formation express consistent orientations (Figure 8). Whereas readings from within the Bitter Springs Formation yield a much more chaotic pattern (Figure 8). A difference in ductility of formations could be the cause of this, however, it is interpreted that the detachment layer promotes greater amounts of flexural slip during folding, causing an increase in frequency of folds and decrease in wavelength and arc length.

Alternate fracture orientations in the Bitter Springs Formation have arisen from the mechanical decoupling of overlying rocks from the regional stress field, forming conjugate fracture sets that infer a strike-slip, transpressional stress regime (Anderson 1951). Paleo-stress orientations are not consistent over the three transects, suggesting that a rotation in principal stress orientation arises when the detachment layer is approached. This was observed along the Arltunga Road transect (Figure 13), where fractures indicate a transition from a normal fault stress regime, to east-west directed transpression, to north-south directed transpression, as the detachment layer was approached. Therefore rocks that are proximal to the detachment layer are inferred to experience near-field stress deformation and hence contain structures that are not conformable with rocks higher in the stratigraphy (Morley & Guerin 1996, King *et al.* 2009).

Folding in the Amadeus Basin is extensive. Comparison between fold geometries and detachment proximity has led to the conclusion that fold amplitudes will decrease as the vertical distance from the detachment is increased. This relationship is replicated in measurements of folds from cross-sections. This also applies for fold wavelengths and arc lengths. Overall, this is greatly increasing the frequency of folds, and would explain the increased complexity of structural geometries along the Arltunga Road transect (Figure 13). This is consistent with other studies of a detachment in Mexico, where complexly deformed evaporites outcrop in the hinges of the large Portrero Chico anticlines, whereas the surrounding limbs express a simple structure (Latta & Anastasio 2007). However, we are seeing this affect on a much larger scale.

Overall, shortening has the strongest relationship with detachment proximity. Figure 23 distinctly shows the transition from non-salt influence shortening to salt-influenced shortening. The amount of shortening in layers above the detachment decreases as salt-cored antiforms appear in the seismic data. This concludes the fact that the detachment layer would be compensating for a majority of the compressive stresses in these regions, more specifically the within a 1.5 km radius, as illustrated from shortening estimates from field data as well (Figure 26).

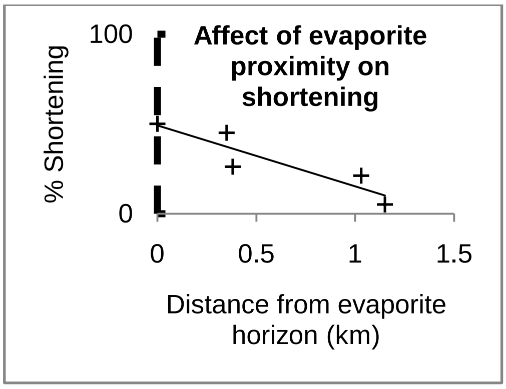

Figure 26. Shortening estimates from filed data for within 1.5 km proximity to detachment layer.

Detachment Thickness

Salt has long been known to perturb stress fields (Birchwood & Noeth 2012), which arises from a difference in competency and density between layers (Mitra 2003). This interface of competent to incompetent rocks will, therefore, be affected by the thickness of the salt column that is present during deformation.

Aspect ratio analysis of salt-cored antiforms reveals that changes in thickness do indeed alter the geometry of folds. Thicker salt columns lead to larger aspect ratios which, in turn, lead to an increase in amplitude and wavelength. This process can be described by typical detachment folding, whereby increased amounts of compression lead to isoclinal geometries of folds (Mitra 2003).

Overlying formations along the Loves Creek and Arltunga Road transects indicate very low values of shorting. It is interpreted that this is because the volume of salt beneath these layers was very large, due to synformal deflection from beneath the Ross River Syncline (Figure 7b). This syncline is interpreted to have caused major salt evacuation into the north, therefore heavily detaching rocks and subsequently causing symmetric folds with simple geometries such as folds AL1 and SL1 in the Loves Creek transect (Figure 12).

The extent of salt evacuation beneath the Ross River Syncline has been linked to the large back-thrust at Trephina Gorge (Figure 14). An absence of salt between competent layers would cause grounding, forcing these rocks together. This contact would permit the propagation of large thrust faults through the now absent detachment layer, creating large amounts of exhumation. It has therefore been interpreted that the salt supply has been exhausted beyond Trephina Gorge. A large back-thrust is also present along the Arltunga Road transect (Figure 14), however vertical throw was not sufficient enough to exhume the Heavitree Quartzite, thus there was some volume of salt present in this region during deformation. As no large thrust faults were observe in formations that overly the Bitter Springs Formation, it is apparent that the presence of a detachment will cease the propagation of thrust faults.

These interpretations have been made on results that are subject to human error. Field data was taken with care, however, measurements are expected to have an error of ± 5˚. Salt horizons in seismic have a characteristic diffraction phenomena, as well as hyperbolic events that mask underlying layers (Tay, 2002). This may result in a mis-interpretation of structures within the seismic lines, as these were the layers that were being studied. The seismic itself was shot in the 1960’s and has quite poor resolution.

The poor resolution may affect the scale and geometry of folds interpreted herein. However, this affect is not of a magnitude that could disprove the final interpretations and conclusions stated herein.

CONCLUSIONS

Heterogeneities in thickness of a detachment horizon appear to directly affect the structures formed above and below it during compressional deformation. A thick, incompetent layer of salt will completely mechanically decouple the overlying packages of rock from the regional stress field, thereby producing folds with no vergence, and preventing a systematic orientation of bedding in the area. In areas such as Trephina Gorge, where the lateral extent of the salt has been exhausted, buttressing of competent layers will result, enabling the propagation of large back-thrust faults with a large dip-slip displacement. Fold size decreases and hence the frequency increases as the detachment layer is approached, and shortening estimates increase as a result. Resolution of seismic and the extent of possible field data that could have been collected have restricted the assurance of some of these conclusions. Depth data and east-west transects in the field would contribute to the understanding of fold geometry and out of plane movement (strike-slip displacement).

ACKNOWLEDGMENTS

This project was supported by a grant from the ARC and would not have happened otherwise. I would like to thank my supervisor, Dr. Rosalind King, for assistance in the field and answering all questions, and providing academic guidance when needed. My peer Owen Girardi for his field assistance. Kathryn Amos, Sandra Mann, Guillaume Backe and Bruce Ainsworth. The owners of the Ross River Resort, Shane and Jodie, for the wonderful hospitality, and PIRSA, DMITRE for providing seismic data. I extend a final thanks to all of my peers, the geology honours class of 2012.

REFERENCES

ANDERSON E. M. 1951. *The dynamics of faulting and dkye formation with applications to Brittain* (2nd edition). Oliver and Boyd Edinburgh.

BIRCHWOOD R. & NOETH S. 2012. Horizontal stress contrast in the shallow marine sediments of the Gulf of Mexico sites Walker Ridge 313 and Atwater Valley 13 and 14 – Geological observations, effects on wellbore stability, and implications for drilling. *Marine and Petroleum Geology* **34**, 186-208.

DAHLSTROM C. D. A. 1990. Geometric constraints derived from the law of conservation of volume and applied to evolutionary models for detachment folding. *AAPG Bulletin* **74**, 336-344.

DAVIS D. M. & ENGELDER T. 1985. The role of salt in fold-and-thrust belts. *Tectonophysics* **119**, 67-88.

DE SITTER L. U. 1964. *Structural Geology* (Second edition). McGraw-Hill, New-York.

DUVAL B., CRAMEZ C. & JACKSON M. P. A. 1992. Raft tectonics in the Kwanza Basin, Angola. *Marine and Petroleum Geology* **9**, 389-404.

FLEUTY M. J. 1964. The Description of Folds. *Proceedings of The Geologists Association* **75**, 461-492.

FLÖTTMANN T. & HAND M. 1999. Folded basement-cored tectonic wedges along the northern edge of the Amadeus Basin, Central Australia: evaluation of orogenic shortening. *Journal of Structural Geology* **21**, 399-412.

HUDEC H. R. & JACKSON M. P. A. 2004. Regional restoration accross the Kwanza basin, Angola: salt tectonics triggered by repeated uplift of a metastable passive margin. *AAPG Bulletin* **88**, 971-990.

HUDEC M. R. & JACKSON M. P. A. 2007. Terra infirma: Understanding salt tectonics. *Earth-Science Reviews* **82**, 1-28.

JACKSON M. P. A., HUDEC M. R., JENNETTE D. C. & KILBY R. E. 2008. Evolution of the Cretaceous Astrid thrust belt in the ultradeep-water Lower Congo Basin, Gabon. *AAPG Bulletin* **92**, 487-511.

KENNEDY M. 1993. The Undoolya sequence: Late Proterozoic salt influenced deposition, Amadeus Basin, central Australia. *Australian Journal of Earth Sciences* **30**, 217-228.

KING R. C., BACKE G., MORLEY C. K., HILLIS R. K. & TINGAY M. R. P. 2010. Balancing deformation in NW Borneo: Quantifying plate-scale vs. gravitational tectonics in a delta and deepwater fold-thrust belt system. *Marine and Petroleum Geology* **27**, 238-246.

KING R. C., HILLIS R. R., TINGAY M. R. P. & MORLEY C. K. 2009. Present-day stress and neotectonic provinces of the Baram Delta and deep-water fold–thrust belt. *Journal of the Geological Society, London* **166**, 197-200.

KORSCH R. J. & LINDSAY J. F. 1989. Relationships between deformation and basin evolution in the intracratonic Amadeus Basin, central Australia. *Tectonophysics* **158**, 5-22.

LATTA D. K. & ANASTASIO D. J. 2007. Multiple scales of mechanical stratification and décollement fold kinematics, Sierra Madre Oriental foreland, northeast Mexico. *Journal of Structural Geology* **29**, 1241-1255.

LI Q., SIMO J. A., MCGOWRAN B. & HOLBOURN A. 2004. The eustatic and tectonic origin of Neogene unconformities from the Great Australian Bight. *Marine Geology* **203**, 57-81.

LINDSAY J. F. 1989. Depositional controls on glacial facies associations in the basinal setting, late Proterozoic, Amadeus Basin, central Australia. *Palaeogeography, Palaeoclimatology, Palaeoecology* **73**, 205-233.

LINDSAY J. F. 1999. Heavitree Quartzite, a Neoproterozoic (ca 800–760 Ma), high-energy, tidally influenced, ramp association, Amadeus Basin, central Australia. *Australian Journal of Earth Sciences* **46**, 127-139.

LONCKE L., GAULLIER V., MASCLE J., VENDERVILLE B. & CAMERA L. 2006. The Nile deep-sea fan: an example of interacting sedimentation, salt tectonics, and inherited subsalt paleotopographic features. *Marine and Petroleum Geology* **23**, 297-315.

MARSHALL T. R. & WILTSHIRE R. G. 2007b. Evaporite flow folds: Characterisation and mechanics from outcrop in the Amadeus Basin, central Australia. **in Munson TJ and Ambrose GJ (editors) 'Proceedings of the Central Australian Basins Symposium (CABS), Alice Springs, Northern Territory, 16–18 August, 2005.' Northern Territory Geological Survey, Special Publication 2**.

MITRA S. 2003. A unified kinematic model for the evolution of detachment folds. *Journal of Structural Geology* **25**, 1659-1673.

MORLEY C. K. & GUERIN G. 1996. Comparison of gravity-driven deformation styles and behavior associated with mobile shales ans salt. *Tectonics* **15**.

MORLEY C. K., KING R., HILLIS R., TINGAY M. & BACKE G. 2011. Deepwater fold and thrust belt classification, tectonics, structure and hydrocaron prospectivity: A review. *Earth-Science Reviews* **104**, 41-91.

OZIMIC S., PASSMORE V., PAIN L. & LAVEERING I. 1986. Australian Petroleum Accumulations Report 1: Amadeus Basin, central Australia. *Bureau of Mineral Resources, Geology and Geophysics*.

PREISS W. V., WALTER M. R., COATS R. P. & WELLS A. T. 1978. Lithologic correlations of Adelaidean glaciogenic rocks in parts of the Amadeus, Ngalia, and Georgina Basins. *Bureau of Mineral Resources Journal of Australian Geology and Geophysics* **3**, 45-53.

ROERING C. 1968. The geometrical significance of natural en-echelon crack-arrays. *Tectonophysics* **5**, 107-123.

ROWAN M. G., PEEL F. J. & VENDERVILLE B. C. 2004. Gravity-driven fold belts on passive margins. *In: McClay. K., Thrust Tectonics and Hydrocarbon Systems: AAPG Mem.,* **82**, 157-182.

SHAW R. D. & ETHERIDGE M. A. 1991. Development of the Late Proterozoic to Mid-Paleozoic, intracratonic Amadeus Basin in Central Australia: A key to understanding tectonic forces in plate interiors. *Tectonics* **10**, 688-721.

SKOTNICKI T. J., HILL A. C., WALTER M. & JENKINS R. 2008. Stratigraphic relationships of Cryogenian strata disconformably overlying the Bitter Springs Formation, northeastern Amadeus Basin, Central Australia. *Precambrian Research* **165**, 243-259.

STEWART A. J. 1979. A barred-basin marine evaporite in Upper Proterozoic of the Amadeus Basin, Central Australia. *Sedimentology* **26**, 33-62.

TINGAY M. R., BENTHAM P., DE FEYTER A. & KELLNER A. 2010. Present-day stress field rotations associated with evaporites in the offshore Nile delta. *Geological Society American Bulliten*.

TRUDGILL B. D., ROWAN M. G., FIDUK J. C., WEIMER P., GALE P. E., KORN B. E., PHAIR R. L., GAFFORD W. T., ROBERTS G. R. & DOBBS S. W. 1999. The Perdido Fold Belt, Northwestern Deep Gulf of Mexico, Part 1: Structural Geometry, Evolution and Regional Implications. *AAPG Bulletin* **83**, 88-113.

TWISS R. J. & MOORES E. M. 1992. *Structural Geology*. W.H. Freeman and Company, New York.

WALTER M. R., VEEVERS J. J., CALVER C. R. & GREY K. 1995. Neoproterozoic stratigraphy of the Centralian Superbasin, Australia. *Precambrian Research* **73**, 173-195.

WELLS A. T., FORMAN D. J., RANFORD L. C. & COOK P. J. 1970. Geology of the Amadeus Basin, central Australia. *Bureau of Mineral Resources Geology and Geophysics, Australia* **100**, 222 pp.

WESTE G. 1990. Northern Territory Geological Survey petroleum basin study - Eastern Amadeus Basin. *Government Printer of the Northern Territory, Darwin*.

APPENDIX A: SEISMIC LINE DETAILS

APPENDIX B: TABULATED FIELD DATA

APPENDIX C: FIELD NOTEBOOK

APPENDIX A: SEISMIC LINE DETAILS

Survey Name	line	Data type	Client	Area	Record Length	Shot Points	Processing	Record width
WEST	0-7	Two-way time				1321.00		29.24
	P81-J14	Two-way time				714.00		18.86
	M87-TA01	Two-way time				12739.00		9.96
	P82-GE41	Two-way time				9836.00		20.74
	M83-05	Two-way time				555.00		7.71
	M83-13	Two-way time				579.00		6.95
	M82-10	Two-way time				348.00		9.07
	M82-11	Two-way time				1007.00		25.27
	P81-U4	Two-way time				8659.00		17.89
	P83-HJ1	Two-way time				29270.00		25.54
	I99A-16	Two-way time				593.00		6.09
	2-5	Two-way time				16659.00		31.68
	2-A	Two-way time				16094.00		30.00
	M94-PV04R	Two-way time				1944.00		14.38
	2-1	Two-way time				11859.00		22.33
	3-5	Two-way time				11575.00		20.00
	3-4	Two-way time				15243.00		29.07
	73-3-3.6	Two-way time				8127.00		13.94
	73-3-AEX	Two-way time				23528.00		52.65
	73-3-2.3	Two-way time				9246.00		22.33
	3-1	Two-way time				15794.00		61.25
	3-2XDX	Two-way time				9151.00		17.40
	P80-2	Two-way time				12870.00		27.36
	P80-4	Two-way time				10517.00		23.57
	MCF81-07	Two-way time				19127.00		41.18
	DH91-2N	Two-way time				2667.00		20.25
	82-01	Two-way time				865.00		21.80
	MR89-102	Two-way time				2006.00		12.62
EAST	82-06	Two-way time				486.00		13.12

APPENDIX B: TABULATED FIELD DATA

Stop	Long (E)	Lat (S)	Elevation(m)	Lithology	Formation	Fossils	Sed Sructure	Folding	Dip	D Direc		A Plane	Fold Plunge	Fault	Fracture	Slicks	Drawing	Picture
LM1	134.48799	23.59935	486.1	Sandstone	Arumbra		Planar CB		40	183					60/030		yes	no
															50/029			
															55/032			
LM2	134.4860	23.6005	481.7	Blocky Quartzite	Arumbra				39	184					62/020		yes	no
									34	182					69/037			
															64/313			
															72/327			
															56/042			
															80/308			
LM3	134.4860	23.6006	No Data	Dark Brown SST	Arumbra		Planar CB		33	182							yes	no
LM4	134.4859	23.6014	481	Dolomite	Top Arumbra?		Planar CB		33	189					46/000		yes	no
									29	186					58/042			
															46/000			
															49/079			
															52/009			
															72/118			
LM5	134.48680	23.60230	539.8	Dolomite					32	181							no	no
LM6	134.48670	23.60288	494.9	Dolomite					38	200							no	no
LM7	134.48519	23.60305	479.9	Dolomite					20	200							no	no
LM8	134.48689	23.60394	483.1	Dolomite		Algal			39	184							no	no
						Menazoin												
LM9	134.48743	23.60536	494.5	Dolomite					38	186							no	no
LM10	134.48793	23.60551	483.2	Dolomite					28	180							no	no
									28	170								
LM11	134.49262	23.60564	479.5	Dolomite					56	206							no	no
LM12	134.49302	23.60786	492	Dolomite					39	196							no	no
									35	199								
									36	199								
LM13	134.49235	23.61040	494.4	Dolomite		Algal	Pock Marks		30	199							no	no
LM14	134.48963	23.61508	474.9	Dolomite		Algal	Planar CB		38	218							no	13
LM15	134.48924	23.61744	483.1	Medium SST			Planar CB		40	210							no	no
LM16	134.48954	23.61791	477.8	Medium SST/Quartzite													yes	no
LM17	134.48946	23.61854	471.7	Medium SST				yes	36	184							yes	14
									64	117								
									42	31								
LM18	134.49224	23.61615	478.7	SKETCH													yes	15
LM19	134.48962	23.61899	473.5	Medium SST/Calcareous/Quartzite			Pock Marks		22	207								16
							Planar CB											17
LM20	134.48971	23.61942	484.9	Medium SST/Calcareous/Quartzite			FAULT	yes	41	256				33/153			yes	no
									83	306				49/207				
									50	265				46/201				
									30	230								
									13	198								
LM21	134.48987	23.61963	474.3	Medium SST/Calcareous/Quartzite				yes	37	138					89/164	pl 36/186	yes	18
									50	331					65/058	pi 20 E		
									27	144								
									54	298								
									22	232								
									86	316								
LM22	134.49005	23.62018	474.4	SST on Dolomite	Arumbra over Goyder				35	268							yes	no
									38	293								
LM23	134.49028	23.62029	462.6						35	244				48/213			no	19

									32	274						
LM24	134.49043	23.62059	473.6						45	309		62/215		yes		21
									32	263		69/231				22
									43	299		72/056				
									52	296		31/291				
								yes	54	297	86/310					
									62	301	39/203					
									79	158						
									28	302						
LM25	134.49089	23.62084	477.7		Shannon		ripples	yes	43	292	21/210			yes		23
									85	312	11/205					
									58	299						
									45	286						
LM26	134.49371	23.62345	476.6	Dolomite	Giles Creek				42	292				no	no	
LM27	134.49320	23.63479	469	Dolomite	Giles Creek				65	238				no	no	
LM28	134.48905	23.65115	504.3	SST/Quartzite	?		Planar CB		22	182				no	no	
									10	150						
									14	165						
LM29	134.48882	23.65918	452.7	SST/Quartzite			Trough CB		8	0				no	no	
									7	305						
LM30	134.49098	23.66578	495.2	SST/Quartzite					20	0						
LM31	134.49126	23.59482	486.3	Dolomite	Julie Formation		Planar CB		30	186			72/020	no	no	
													63/023			
													88/288			
													87/304			
													82/305			
LM32	134.49213	23.59451	469.7	Dolomite/Conglor	Julie Formation				27	196			85/061	yes	no	
													89/280			
													66/062			
													68/012			
LM33	134.43066	23.56314	512.3	Dolomite	BSF		Iron Alteration		41	204			86/131	no	no	
									36	220			84/104			
													83/112			
LM34	134.44112	23.56062	517.3	Dolomite/Conglor	BSF	Algal			34	160						
LM35	134.43978	23.55861	544	Dolomite	BSF			yes	26	265		28/248		yes	no	
									35	217		26/260				
									40	259		26/226				
									40	291		52/017				
									60	265						
									38	220						
									38	232						
									58	245						
									34	210						
									39	198						
									32	228						
LM36	134.43981	23.55858	No Data	Dolomite	BSF			yes	14	268		32/217				
									44	235		86/126				
LM37	134.44267	23.56073	512.3	Dolomite	BSF				21	204				no	no	
LM38	134.44321	23.55939	511	Dolomite	BSF			yes	56	152			90/069	yes		36
									40	114			90/249			37
									49	151			60/269			
									50	130			38/309			
									31	187			58/240			

								45	131							
								57	171							
								48	140							
								53	181							
LM39	134.44378	23.55881	514.2	Dolomite	BSF			37	132		36/097		pl 36/097	yes		
								46	112				pi 20 N			
LM40	134.44383	23.55845	516.1	Dolomite	BSF		yes	24	129		44/060			yes		39
								40	90		42/078					
								40	126							
								38	80							
								24	174							
LM41	134.44573	23.55701	518.2	Dolomite	BSF			51	193					yes		41
LM42	134.44605	23.55682	514.8	Dolomite	BSF		yes	30	66	71/206				yes		42
								22	49							43
								53	207							
								58	19							
								27	187							
LM43	134.44622	23.55639	530.9	Dolomite	BSF			38	25		33/050			yes		44
								48	22		40/021					45
								42	41							
								57	27							
LM44	134.44844	23.55646	520.3	Dolomite	BSF	Fe Alteration		70	224			62/129		yes		46
								63	239			50/327				47
												20/353				
LM45	134.44888	23.55647	530.3	Dolomite	BSF	Planar CB		70	226					yes		48
LM46	134.44894	23.55607	531.3	Dolomite + Brecci	BSF			37	316					no		49
								49	321							
LM47	134.44919	23.55599	546.8	Dolomite	BSF		yes	30	327			30/011		yes		50
								39	293			37/018				
								28	316							
								32	340							
LM48	134.44935	23.55595	552.9	Dolomite	BSF		yes	14	104			44/310		yes		51
								22	359			86/304				52
								33	355			31/329				
								5	315							
								70	327							
								18	13							
LM49	134.44950	23.55588	552.8	Dolomite	BSF		yes	42	117	58/114				yes	no	
								86	317							
LM50	134.45006	23.55573	567.4	Dolomite	BSF		yes	48	3	88/021	17/040	80/018		yes		53
								28	5	84/186		78/130				54
								52	181							55
								19	160							56
								32	170							57
								40	353							
								72	186							
LM51	134.45005	23.55552	576.7	Dolomite	BSF		yes	50	41			74/347		yes		58
								60	7							
LM52	134.45020	23.55530	578.5	Dolomite	BSF		yes	56	174			72/182				
								40	130			61/054				
								27	78							
								40	353							
								68	277							

									38	23							
LM53	134.45064	23.55440	598.4	Dolomite	BSF	Stroms			30	24				84/355	yes		59
														62/104			
														89/166			
LM54	134.45093	23.55423	605.1	Dolomite	BSF	Stroms			32	319				60/110	no	no	
LM55	134.45107	23.55385	589.7	Dolomite + Scree	BSF			yes	16	310					yes		
									49	347							
									19	314							
LM56	134.45098	23.55366	575.1	Dolomite	BSF				35	334			90/008	90/320	yes	no	
									41	3				90/140			
									10	256				70/083			
														69/173			
LM57	n/a	n/a	n/a	Dolomite	BSF				21	275					no	no	
LM58	134.45110	23.55329	572.2	Dolomite	BSF			yes	1	59			84/174	24/321	yes	no	
									85	348				32/084			
									40	39				61/160			
									51	346							
									64	352							
									40	204							
									90	359							
									40	284							
LM59	134.45214	23.55343	582.5	Dolomite	BSF			yes	19	46					no	no	
									39	319							
LM60	134.45452	23.55433	520.9	Dolomite + Cataclasite					37	21					no		68
																	69
																	70
LM61	134.45163	23.55364	545.4	Dolomite	BSF				50	345				88/009	yes		71
									20	311							
									38	339							
									41	339							
LM62	134.45167	23.55330	559.1	Dolomite	BSF	Stroms		yes	47	3					no	no	
LM63	134.45166	23.55310	575.3	Dolomite + Siltsto	BSF			yes	48	9	80/258	north			yes	no	
									41	354							
									47	28							
LM64	134.45150	23.55262	602.3	Smooth rock -myl	BSF			yes	61	35	68/074						72
									71	115							73
									70	304							74
									42	45							
LM65	134.45175	23.55266	596	Dolomite + Smoot	BSF			yes	58	34					yes		75
									79	221							
LM66	134.45166	23.55257	606.9	Dolomite	BSF			yes	85	26					yes		76
																	77
LM67	134.45230	23.55276	582.2	Dolomite	BSF		Fe Alteration		21	156					no	no	
LM68	134.45273	23.55242	556.5	Dolomite+ Shale +	BSF		Crystals	yes	39	220					yes		78
							Onlap pebble		61	204							79
							Soft Sed def		56	200							80
LM69	134.45293	23.55170	527.8	Fault Breccia													
LM70	134.45338	23.55099	527.6	Fault Breccia													
LM71	134.45382	23.55042	524.2	Dolomite + thin sh	BSF				69	10							
LM72	134.45404	23.54880	527.1	Breccia													
LM73	134.45459	23.54826	538.4	Contact between breccia and Dol					58	17							
LM74	134.45467	23.54794	549	Dolomite + some	BSF										yes		81
																	82

LM75	134.45520	23.54744	568.5	Dolomite	BSF			42	38					
LM76	134.45555	23.54715	574.4	Dolomite	BSF		yes	44	93			yes		83
								26	32					
								32	121					
LM77	134.45582	23.54675	590	Dolomite	BSF		wavy	37	64			no	no	
LM78	134.45620	23.54656	592.5	Conglomerate	Areyonga?									
LM79	134.45640	23.54667	600	Dolomite + Congl	BSF			48	165			no		84
														85
														87
LM80	134.45647	23.54616	587.1	Conglomerate				41	100					
LM81	n/a	n/a	n/a	Dolomite	BSF			39	134					
LM82	134.45737	23.54573	576.6	Dolomite	BSF		yes	23	178	22/004	78/316	yes		86
								32	355		77/336			
								1	194					
								42	343					
LM83	134.45741	23.54526	597.9	Dolomite - Heavily	BSF			22	89					
LM84	134.45753	23.54506	604.6	Dolomite	BSF			22	45					
								72	1					
LM85	134.45764	23.54458	596.4	Conglom + Dolom	BSF/Areyonga			42	20					
LM86	134.45791	23.54425	596.4	SST + silt + dol	Bottom Areyonga			38	38			no	no	
LM87	134.45820	23.54405	617.7	SST Conglomerate			yes	18	36			no	no	
								22	37					
								62	188					
								85	5					
LM88	134.45830	23.54371	608.7	Dolomite	Areyonga									
LM89	134.45863	23.54340	585.5	Breccia SST	Areyonga							no	no	
LM90	134.45705	23.55416	518.7	Dolomite	BSF			60	99			yes		89
LM91	134.45680	23.55411	526	Dolomite	BSF			80	56			yes	no	
								41	314					
								82	86					
LM92	134.45648	23.55369	559.2	Dolomite	BSF			68	208			no	no	
LM93	134.39643	23.51761	544.1	Dark Brown Quart	Heavitree			10	46		68/149	yes		90
											58/146			
LM94	134.39675	23.51850	564.5	Dark Brown Quart	Heavitree			20	109		28/144	yes		91
											64/076			
LM95	134.39724	23.51924	538	Dark Brown Quart	Heavitree	Symetric rips		12	102			no	no	
LM96	134.39888	23.52005	557	Massive Calcearei	Heavitree/BSF	FE Alteration						no	no	
LM97	134.39941	23.52015	591.9	Contact - Slaty sh	BSF	Planar CB		22	124					92
												yes		93
														94
														95
LM98	134.39737	23.51998	549.7	Quartzite	Heavitree			19	143		82/051	yes		96
											74/282			
LM99	134.39665	23.52078	567.4	Quartzite	Heavitree	Ripples		28	138		58/340	no	no	
											75/059			
LM100	134.39582	23.52121	555.7	Quartzite	Heavitree		yes	30	16			yes	no	
LM101	134.39548	23.52191	553.6	Dolomite	BSF	Planar CB		55	188			no	no	
LM102	134.39512	23.52219	572.4	Dolomite	BSF		yes	80	176		58/276	yes		97
								62	5					
LM103	134.39509	23.52247	563.6	Dolomite	BSF			25	32			no	no	
								57	359					
LM104	134.38873	23.52529	555.3	Dolomite	BSF			38	74			no	no	
LM105	134.38839	23.52585	589.5	SST/Quartzite	Heavitree or Areyo?									

														yes		98
LM106	134.38733	23.52838	556.4	Coarse Arkose	Areyonga or HTQ									no	no	
LM107	134.38711	23.52912	546.8	Dolomite	BSF									no	no	
LM108	134.38673	23.52971	555.2	Dolomite	BSF		yes	80	220	72/323				yes		99
								80	187							
								89	59							
LM109	134.38609	23.53011	591.9	Dolomite	BSF			6	206				80/311	no	no	
LM110	134.38572	23.53051	611.1	Dolomite	BSF		yes	62	44				83/132	no	no	
LM111	134.38560	23.53044	615.2	Dolomite	BSF		yes	70	255	28/012				yes		100
								60	52							
								76	249							
								44	265							
LM112	134.38538	23.53042	626.5	Dolomote	BSF			4	277				82/181	yes		103
													71/101			104
																105
LM113	134.38350	23.53634	535.4	Dolomite	BSF		yes				trend 070			yes		107
LM114	134.38467	23.53435	532.6	Dolomite	BSF			42	88					no	no	
LM115	134.38493	23.53469	535.8	Dolomite	BSF			22	24					no	no	
LM116	134.38523	23.53501	530.2	Dolomite	BSF			36	39					no	no	
LM117	134.3758	23.5457	561.2	Dolomite	BSF		yes	30	201			83/229		yes		108
								73	206							
								30	199							
								27	167							
								18	214							
								16	231							
LM118	134.37549	23.54622	557.6	Dolomite	BSF			29	98				72/313	no	no	
													78/219			
LM119	134.37497	23.54672	553.3	Dolomite	BSF			18	2					no	no	
LM120	134.37478	23.54699	559	Dolomite	BSF			65	119				38/210	no	no	
													60/009			
LM121	134.3747	23.54713	566.3	Dolomite	BSF			39	251				70/334	yes		109
													82/197			
													40/275			
LM122	134.37427	23.55901	542.7	Dolomite/shale	BSF	Trough CB		43	72				43/218	no		110
													81/334			
													69/334			
LM123	134.37372	23.56199	557.4	Dolomite	BSF		yes	80	180				50/083	yes	no	
LM124	134.37375	23.56206	564.2	Dolomite	BSF		yes	78	180				30/306	no	no	
								79	170				51/069			
LM125	134.37403	23.5621	576.7	Dolomite	BSF			70	228				58/089	no	no	
													15/219			
LM126	134.37366	23.56238	541.4	Dolomite	BSF		yes	36	126				80/015	no	no	
													62/309			
LM127	134.37405	23.56265	531.2	Dolomite	BSF		yes	65	29			Thrust		yes		111
												WSW				112
LM128	134.37241	23.56285	538.9	Dolomite	BSF		yrd							yes		113
																114

APPENDIX C: FIELD NOTEBOOK